J Mater Sci (2025) 60:1826–1852

Ceramics

Correlation between grain-boundary segregation behaviors of calcium and yttrium and enhanced fracture toughness in magnesium aluminate spinel

Alexander Campos-Quiros[1,*], Metri Zughbi[1], Animesh Kundu[2], and Masashi Watanabe[1,3,*]

[1] Department of Materials Science and Engineering, Lehigh University, 5 East Packer Avenue, Bethlehem, PA 18015, USA
[2] Department of Mechanical Engineering and Mechanics, Lehigh University, 19 Memorial Drive West, Bethlehem, PA 18015, USA
[3] Institute for Materials Research, Tohoku University, 2-1-1 Katahira, Aoba-ku, Sendai, Miyagi 980-8577, Japan

Received: 26 September 2024
Accepted: 20 December 2024
Published online: 3 January 2025

ABSTRACT

Polycrystalline magnesium aluminate spinel, or simply spinel, with near theoretical density is a transparent ceramic material with multiple applications in extreme environmental conditions, which require an enhanced fracture toughness. For this reason, in this study, the effect of 500 ppm doping level of calcium (Ca) and yttrium (Y) on the segregation behavior and mechanical properties of spinel was quantitatively investigated. Calcium and yttrium doping reduced the grain-boundary plane anisotropy for grain boundaries with rotations about the [111] axis. More tilt boundaries and fewer twist boundaries were found in the doped samples compared to the undoped condition. Direct observations by high-angle annular dark-field scanning transmission electron microscopy (HAADF-STEM) imaging revealed that yttrium atoms preferentially occupy aluminum sites at grain boundaries in spinel. Quantitative electron energy-loss spectrometry (EELS) analysis in the vicinity of grain boundaries indicated that calcium atoms preferentially occupy magnesium sites in the Ca-doped spinel samples and confirmed the substitution of aluminum by yttrium atoms in the Y-doped sample. Quantitative X-ray energy-dispersive spectrometry (XEDS) analysis employing the ζ-factor method indicated that the maximum segregation levels at grain boundaries were 0.8 ± 0.1 calcium atoms/nm^2 (0.23 ± 0.03 monolayers) and 2.4 ± 0.06 yttrium atoms/nm^2 (0.45 ± 0.11 monolayers). Enhanced indentation fracture toughness was found in samples with calcium and yttrium doping compared to undoped spinel. The enhanced fracture toughness in Ca- and Y-doped spinel samples, in comparison with undoped spinel, was primarily attributed to more pronounced crack deflections and a more tortuous crack path.

Handling Editor: David Cann.

Address correspondence to E-mail: ajc420@lehigh.edu; masashi.watanabe@lehigh.edu

https://doi.org/10.1007/s10853-024-10569-9

GRAPHICAL ABSTRACT

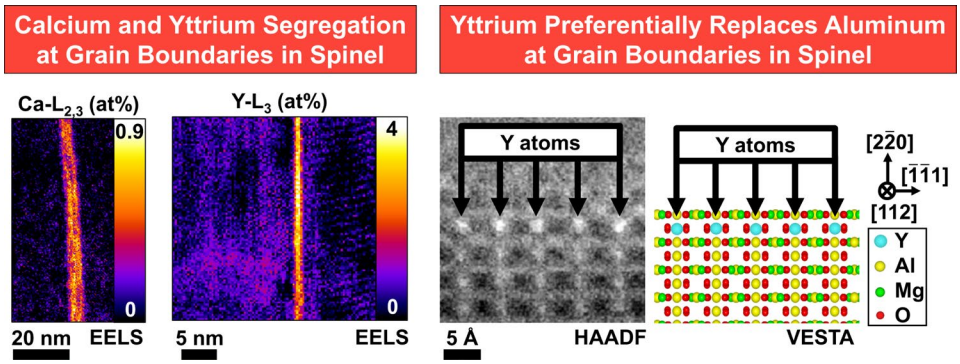

Introduction

Polycrystalline magnesium aluminate spinel ($MgAl_2O_4$), or simply spinel, with near theoretical density is a transparent ceramic material of great interest for application in extreme environments where high mechanical integrity, low density, thermal and corrosive resistance, and high transparency are required [1]. Some relevant applications of spinel include transparent ceramics for aircraft windows, sensor protection, multispectral and ultra-violet windows, transparent domes, ballistic-resistant windows, radiation-resistant windows and refractory materials [2]. For many of these applications, high fracture toughness has been identified as a critical mechanical property to be achieved [3].

One common strategy for enhancing fracture toughness in ceramic materials involves the introduction of secondary phases promoting crack deflection and crack bridging [4]. However, the secondary phases can act as scattering sites for transmission of electromagnetic radiation resulting in a loss of optical transparency. In another approach, controlled grain-boundary segregation in small amounts has been reported to enhance grain-boundary cohesion and consequently increase fracture toughness [5–8]. Such a small amount of segregation is expected to have a small effect on the optical transmission. This strategy could potentially aid in achieving an optimal balance between mechanical performance and optical transparency in spinel, which has been proven to be the major obstacle for practical applications.

Dopants serve multiple purposes in ceramic processing such as a sintering aid [9], control the kinetics of grain growth [10], modify the grain-boundary population and energy [11] and enhance certain mechanical properties [12]. Often, the addition of small amounts of a dopant (typically in the order of part per million or ppm) is sufficient for desired effects [13]. The dopants, or solute atoms, can segregate to the interfaces such as grain boundaries where they can occupy lower energy sites compared to the bulk [14]. However, selecting dopants to achieve an enhanced grain-boundary cohesion, and fracture toughness, in spinel remains a challenging task. Cui et al. have demonstrated that doping spinel bi-crystals with europium (Eu^{2+}) had no significant effect on the fracture toughness of individual grain boundaries measured by micromechanical testing, despite clear observations of grain-boundary segregation by electron microscopy analysis [15]. Conversely, Cao et al. found that doping with ytterbium (Yb^{3+}), a different rare-earth element, increases the fracture toughness measured by microcantilever bend testing by 30% compared to the undoped bi-crystal [8]. Despite these advances in understanding the segregation behavior of rare-earth dopants in spinel, the atomic-scale mechanism of enhanced grain-boundary fracture toughness remains not well understood yet. Moreover, more inexpensive and earth-abundant dopants are desirable for the mass production of spinel parts, instead of rare-earth dopants. For this reason, alternative dopants require more investigation.

Based on previous studies [8, 15], it is hypothesized that dopants must satisfy three main conditions for an effective grain-boundary strengthening effect. First, the dopant atoms must have a larger ionic radius as compared to host cations magnesium and aluminum (Mg^{2+} (r_i = 57 pm in tetrahedral site) and Al^{3+} (r_i = 53 pm in octahedral site) [16]).

The larger ionic radius of the dopants compared to host cations makes grain-boundary segregation favorable as substitution in the lattice is unlikely due to the high elastic strain that this represents. Second, the dopants must have lower formation energies for oxides compared to magnesium and aluminum. Dopants with lower formation energies for oxides, i.e., stronger bonding with oxygen atoms, are expected to increase the grain-boundary cohesion compared to host cations magnesium and aluminum due to their high affinity to form bonds with oxygen. Third, the dopants with 3 + oxidation states are more effective at enhancing the fracture toughness than 2 + cations. The effect of the oxidation state on the fracture toughness could be related to the position dopants occupy at the grain boundaries. Ytterbium with a 3 + valence state has been found to occupy both magnesium tetrahedral and aluminum octahedral sites in spinel forming staggering pairs [8]. In contrast, europium with a 2 + oxidation state has been found to preferentially occupy aluminum octahedral sites at grain boundaries [15, 17].

Two promising candidates that satisfy the aforementioned conditions are calcium and yttrium. Both these elements have larger ionic radii compared to host cations, 100 pm for calcium and 90 pm for yttrium, as compared to 57 pm for magnesium and 53 pm for aluminum [16]. Both calcium and yttrium have been reported to segregate at grain boundaries in spinel [18–20]. Moreover, calcium and yttrium present lower formation energy of oxides compared to magnesium and aluminum [21]. Additionally, the difference in the oxidation state provides an opportunity to study the effect of cations with 3 + and 2 + oxidation states on the fracture toughness in spinel.

Previous studies have found that calcium doping increases the bulk fracture toughness of spinel measured by the Vickers indentation method [22]. However, the doping concentration was not controlled and instead a calcium infiltration method was used. Also, the formation of calcium hexaluminate as a secondary phase hindered the isolated effect of calcium segregation on the fracture toughness. Similarly, doping with 2 wt.% of Y_2O_3 has been found to increase the creep resistance [23] and the cold modulus of rupture [12] in spinel. In this case, the enhanced mechanical properties were attributed to the formation of the secondary phase yttrium aluminum garnet. The effects of calcium and yttrium segregation behaviors on the mechanical properties in spinel remain unknown.

In this study, a well-controlled doping level 500 ppm of calcium and yttrium was used to evaluate the effect on the segregation behaviors and mechanical properties in spinel without the presence of secondary phases. Microstructure observations by scanning electron microscopy (SEM) and high-angle annular dark-field scanning transmission electron microscopy (HAADF-STEM) imaging confirmed that no secondary phases were formed at the micro- or nanoscale after doping. Detailed quantitative analysis by electron energy-loss spectrometry (EELS) and X-ray energy-dispersive spectrometry (XEDS) of individual grain boundaries was performed in an aberration-corrected STEM instrument to quantify the segregation behaviors of calcium and yttrium. The fracture behavior with and without doping was evaluated by quantitative electron backscatter diffraction (EBSD) analysis of cracks induced by Vickers microhardness testing. Finally, indentation fracture toughness measurements were performed and the mechanism of how these two dopants affect the mechanical properties were discussed in terms of the segregation behaviors at grain boundaries.

Experimental

Sample fabrication

High-purity spinel powder (Baikowski, S25CR), $Ca(NO_3)_2{\cdot}4H_2O$ (99.98%, Alfa Aesar) and $Y(NO_3)_3{\cdot}4H_2O$ (99.999%, Aldrich Chem. Co.) were utilized in this study. The baseline impurity concentrations of calcium and yttrium in the as-received undoped spinel powder determined by glow discharge mass spectrometry were 5.1 and less than 0.5 ppm by weight, respectively, which are negligible compared to the doping level of 500 ppm used in this study. Also, the Mg/Al ratio was nominally 1.0 in the as-received powder.

First, a specific amount of dopant salts, $Ca(NO_3)_2{\cdot}4H_2O$ and $Y(NO_3)_3{\cdot}4H_2O$, were separately dissolved in high-purity ethanol. The dopant solution (either calcium nitrate or yttrium nitrate) was added to a batch of preweighed spinel powder to produce a suspension with a nominal concentration of 500 ppm by mole of the dopant atom. The doping concentration was selected based on previous studies in spinel doped with rare-earth elements, where doping levels of 500 ppm were observed to be sufficient for affecting

the microstructure and fracture behavior without bulk segregation of second phases [10, 24]. To ensure homogeneous dispersion of the dopants the suspension was thoroughly mixed using a magnetic stirrer. Then, the suspension was dried under a vacuum to remove the excess solvent.

A Thermal Technology LLC hot-press system (HP20-4560-20SS) was employed to fabricate the samples. The undoped spinel and Y-doped spinel powders were hot-pressed individually to near the theoretical density at 1250 °C with 40 MPa applied pressure under vacuum (< 30 mTorr) for 1 h, with heating and cooling rates of 10 °C/min. The dimensions of the hot-pressed samples were nominally 25.4 mm in diameter and 10 mm in height. To avoid contamination from the graphite dies used during the hot-pressing step, only the core of the sample (~ 9 × 9 mm^2) was utilized in this study. The Ca-doped spinel sample in the as-hot-pressed condition was synthesized in a previous study [25] by using the same hot-press procedure described above.

The core of the hot-press samples was sectioned into multiple smaller parts. The microstructure and mechanical properties of as-hot-pressed specimens for each of the undoped, Ca-doped and Y-doped spinel were analyzed to determine the baseline characteristics. Other samples were annealed at 1400 °C for 48 h in an N_2/H_2 atmosphere using a high-purity alumina tube (99.5%), with heating and cooling rates of 5 °C/min. The annealing temperature and time were selected based on previous studies on doped spinels [10]. The segregation behavior of calcium and yttrium atoms to the grain boundaries and its effect on the mechanical properties were studied in detail.

Bulk microstructure

For the bulk microstructural characterization, samples were mechanically polished, followed by finishing with a 50 nm diamond suspension. The porosity and the grain-size distribution of the samples were investigated utilizing SEM coupled with EBSD analysis in a dual beam focused ion beam (FIB) instrument (Thermo/Fisher Scientific Scios). SEM images were acquired at an acceleration voltage of 7 kV with a probe current of 0.8 nA using an in-lens backscattered electron detector. EBSD analysis was performed at an acceleration voltage of 12 kV and a probe current of 13 nA with a step size of 50 nm utilizing an EDAX Hikari camera. EBSD data analysis was performed using EDAX OIM software. A neighbor pattern averaging & reindexing (NPAR™) protocol available within the OIM software was utilized to obtain optimal indexing of the Kikuchi patterns. This was followed by a grain dilation with a minimum grain size of 8 pixels to remove any spurious Kikuchi patterns [26]. For the quantitative grain-size distribution analysis a minimum of 5000 grains were used and incomplete grains from the edges of the EBSD maps were ignored.

Grain-boundary character distributions

Grain-boundary plane distributions (GBPD) and grain-boundary character distributions (GBCD) were calculated from the EBSD results for the samples after heat treatment using the method developed by Saylor et al. [27, 28]. The determination of the GBPD and GBCD relies on multiple observations of grain-boundary line segments extracted from 2-dimensional EBSD maps. The line segments correspond to bi-crystals with undistinguished misorientations. After a statistically significant number of observations, the line segments can be used to estimate the 5 parameters that describe the different grain-boundary types. Then the GBCD can be generated using a stereological projection corresponding to the distribution of grain-boundary normals for a specific axis/angle pair [11, 27, 29, 30].

For the GBPD and GBCD, grain-boundary segments were extracted from the bulk EBSD maps using the OIM software. To minimize the effect of pseudo-symmetry in the EBSD maps, a post-processing step in OIM was introduced to remove pseudo-symmetry around the 60° rotation about the [111] axis, 38.9° rotation about the [110] and 45° rotation about the [100] axes [26]. The number of grain-boundary segments utilized was 41,600, 48,400, and 53,800 for the undoped, Ca-doped and Y-doped spinel samples, respectively. The relative frequency of grain boundaries as a function of the misorientation angle was also calculated.

Segregation behavior

Electron-transparent thin specimens from the samples after heat treatment were prepared using a Ga^+ beam in the Scios FIB instrument operated at 30 kV. Damaged layers on the surface of FIB-prepared thin specimens were gently removed using a Fischione 1040 nanomill instrument at 900 eV. To determine the misorientation angles between grains

in the thin lamellas, transmission Kikuchi diffraction (TKD) analysis was performed using an acceleration voltage of 30 kV, a current of 26 nA, and a step size of 50 nm. To evaluate the dopant segregation behavior, detailed atomic-scale characterization was performed using HAADF-STEM imaging in an aberration-corrected STEM JEOL JEM-ARM200CF instrument operated at 200 kV. XEDS analysis using the ζ-factor method [31] was carried out to quantify the calcium and yttrium excess as a function of the grain-boundary misorientation angle extracted from TKD analysis [32]. The XEDS spectra acquisition was carried out using the raster-scan box method, which consisted of scanning the electron beam over an area of ~ 12 × 75 nm^2 for 120 s. The center of the raster-scan box was aligned with the grain boundary for the on-boundary measurements, ~ 28 nm away from the grain boundary for the off-boundary condition, and several hundreds of nanometers away for the bulk measurements. Magnesium, aluminum, and oxygen concentrations were also determined for all measurements. The number of different grain boundaries analyzed in this study was 14, 20 and 12 for the undoped, Ca-doped and Y-doped spinel samples, respectively.

The grain-boundary excess of calcium and yttrium (Γ_A^{ex}) were determined from the XEDS analysis following the equation [31, 33]:

$$\Gamma_A^{ex} = N_B \frac{X_A^{gb} - X_A^{bk}}{X_B^{bk}} \frac{V}{A} \quad (1)$$

Here, N_B is the number of B atoms per unit volume in the bulk region (either 15.1 Mg atoms/nm^3 or 30.2 Al atoms/nm^3), X_A^{gb} and X_A^{bk} are the atomic fraction of the dopant element A (calcium or yttrium) at the grain boundary and in the bulk region, respectively, X_B^{bk} is the atomic fraction of the element B in the bulk and V and A are the interaction volume and the grain-boundary area inside the interaction volume. The off-boundary measurements (~ 28 nm from the grain boundary) were used for X_A^{bk} and X_B^{bk}, as they did not differ significantly from the bulk measurements.

The selection of element B in Eq. (1) is of key importance in complex oxides such as spinel where two cation sublattices (Mg^{2+} tetrahedral and Al^{3+} octahedral sublattices) are present. For this reason, special attention was paid to elucidating the position of calcium and yttrium atoms at the grain boundaries. Similarly, Eq. (1) was used to calculate the elemental deviations of host cations magnesium and aluminum at the grain boundaries (either excess or depletion). For example, the magnesium deviation was calculated by considering X_A^{gb} as the magnesium concentration on-boundary and X_A^{bk} and X_B^{bk} as the magnesium concentration off-boundary. A similar analysis was used for the aluminum deviation.

To obtain details about the elemental distribution of the different elements in the grain-boundary vicinity, quantitative EELS analysis was performed by acquiring spectrum-imaging (SI) datasets. The EELS analysis was performed through a CEOS energy filtering and imaging device (CEFID) equipped with a hybrid-pixel direct electron detector Dectris ELA. SI datasets were collected with an energy dispersion of 1.77 eV/channel over a range of 1820 eV for undoped and Ca-doped spinel and 3.48 eV/channel over a range of 3580 eV for Y-doped spinel. A convergence semi-angle (α) of 34 mrad and a collection semi-angle (β) of 60 mrad were used with a camera length of 2.5 cm. Furthermore, the SI datasets were acquired using CEOS Panta Rhei software, followed by principal component analysis (PCA) in Gatan Digital Micrograph software to remove random noise [34]. Subsequently, quantitative analysis was performed using the reconstructed SI datasets using the following equation [35]:

$$\frac{N_A}{N_B} = \frac{I_{KA}(\beta, \Delta)\sigma_{JB}(\beta, \Delta)}{I_{JB}(\beta, \Delta)\sigma_{KA}(\beta, \Delta)} \quad (2)$$

Here, N_A and N_B are the areal densities of elements A and B, respectively, $I_{KA}(\beta, \Delta)$ and $I_{JB}(\beta, \Delta)$ are the integrated intensities of the characteristic edges corresponding to elements A and B, respectively, $\sigma_{KA}(\beta, \Delta)$ and $\sigma_{JB}(\beta, \Delta)$ are the partial ionization cross-sections for elements A and B, respectively. The collection semi-angle β (60 mrad) and integration window Δ (34.2 eV) were kept constant, and the subindices K and J denote that different edge families were used depending on the elements A and B energy-losses. Ca-$L_{2,3}$, Y-L_3, O-K, Mg–K, and Al-K edges were used for the quantitative analysis using the Hartree-Slater ionization cross-section model. The errors in the EELS quantitative analysis were estimated considering statistical error following the equation [35]:

$$\Delta C_A = C_A \frac{3\sqrt{I_{KA} + hI_{bA}}}{I_{KA}} \quad (3)$$

$$h = \frac{I_{bA} + 3\sqrt{I_{bA}}}{I_{bA}} \quad (4)$$

Here, ΔC_A is the error associated with the relative composition of the element A, C_A is the relative composition in atomic percent, I_{KA} is the integrated intensity of the edge after background subtraction over the range Δ corresponding to the element A, I_{bA} is the integrated intensity of the background below the integration region of the edge, and h is a dimensionless parameter associated with the uncertainty of the background extrapolation. The factor of 3 in front of the square root terms in Eqs. (3) and (4) indicate the 3σ (3 × standard deviation), i.e., a 99% confidence limit, so that all the errors in this manuscript represent the 3σ.

The high dynamic range of the Dectris ELA detector allowed for the acquisition of the highly intense zero-loss peak (ZLP) simultaneously with the low-intensity edges signals in a single spectrum without saturation. This enabled the calculation of the relative thickness of the specimen using the log-ratio method [35]:

$$t/\lambda = \ln\left(\frac{I}{I_0}\right) \quad (5)$$

Here, t is the specimen thickness, λ is the plasmon mean free path at 200 kV in spinel, I is the total intensity of the spectrum, and I_0 is the zero-loss peak intensity extracted from the SI dataset by fitting the data in the 4–6 eV range with a logarithmic tail model. The relative specimen thickness term t/λ is expressed as a thickness with respect to the inelastic mean free path. All grain boundaries analyzed were performed at regions with relative thickness values below 1, which ensured that the effect of plural scattering was minimized. Hence, plural scattering deconvolution was not applied to the EELS-SI datasets.

Bulk mechanical properties

To determine the effect of both calcium and yttrium doping on the bulk mechanical properties, microindentation hardness measurements were performed following the ASTM-C1327-15 standard [36]. Microhardness measurements were acquired using an applied load of 1 kg, a dwell time of 10 s and a minimum of 30 indentations per sample) in a LECO LM 248AT microhardness tester. The fracture toughness was determined using the Vickers indentation fracture (VIF) method using the following equation [37]:

$$K_c = 0.018\left(\frac{E}{H_v}\right)^{1/2}\left(\frac{P}{c^{3/2}}\right) \quad (6)$$

where K_c is the indentation fracture toughness, E is the elastic modulus (assumed to be 260 GPa for spinel [1]), H_v is the Vickers microhardness, P is the applied load during indentation, and c is the measured length of the cracks that emanate from the tips of the residual Vickers indentation marks. Only indentations with 4 straight primary cracks were used for the fracture toughness determination. Indentations with secondary cracks or spalled edges were disregarded in this analysis.

Crack propagation behavior

The crack propagation behavior analysis around the indentation area was conducted using SEM/EBSD analysis following the same acquisition conditions utilized for the bulk observations. A partition on the image quality was performed to remove the pixels from the crack regions without clear Kikuchi patterns. Subsequently, quantitative analysis was performed on the EBSD data from crack regions to determine the percentage of transgranular fracture. Regions along the crack path with similar colors (similar orientation in the inverse pole figure (IPF) maps) on both sides of the crack were assigned as transgranular, whereas points with different colors were considered intergranular. The fraction of transgranular fracture was calculated as the total length of grain with transgranular fracture divided by the total length of the crack. A minimum of ~ 200 grains along the crack path per sample were analyzed.

Results

Bulk microstructure

Figure 1 shows the EBSD analysis results for the samples after hot-pressing and after annealing treatments at 1400 °C for 48 h. No noticeable grain-orientation texture was found in any of the samples before or after annealing. All samples in the as-hot-pressed condition presented similar average grain sizes

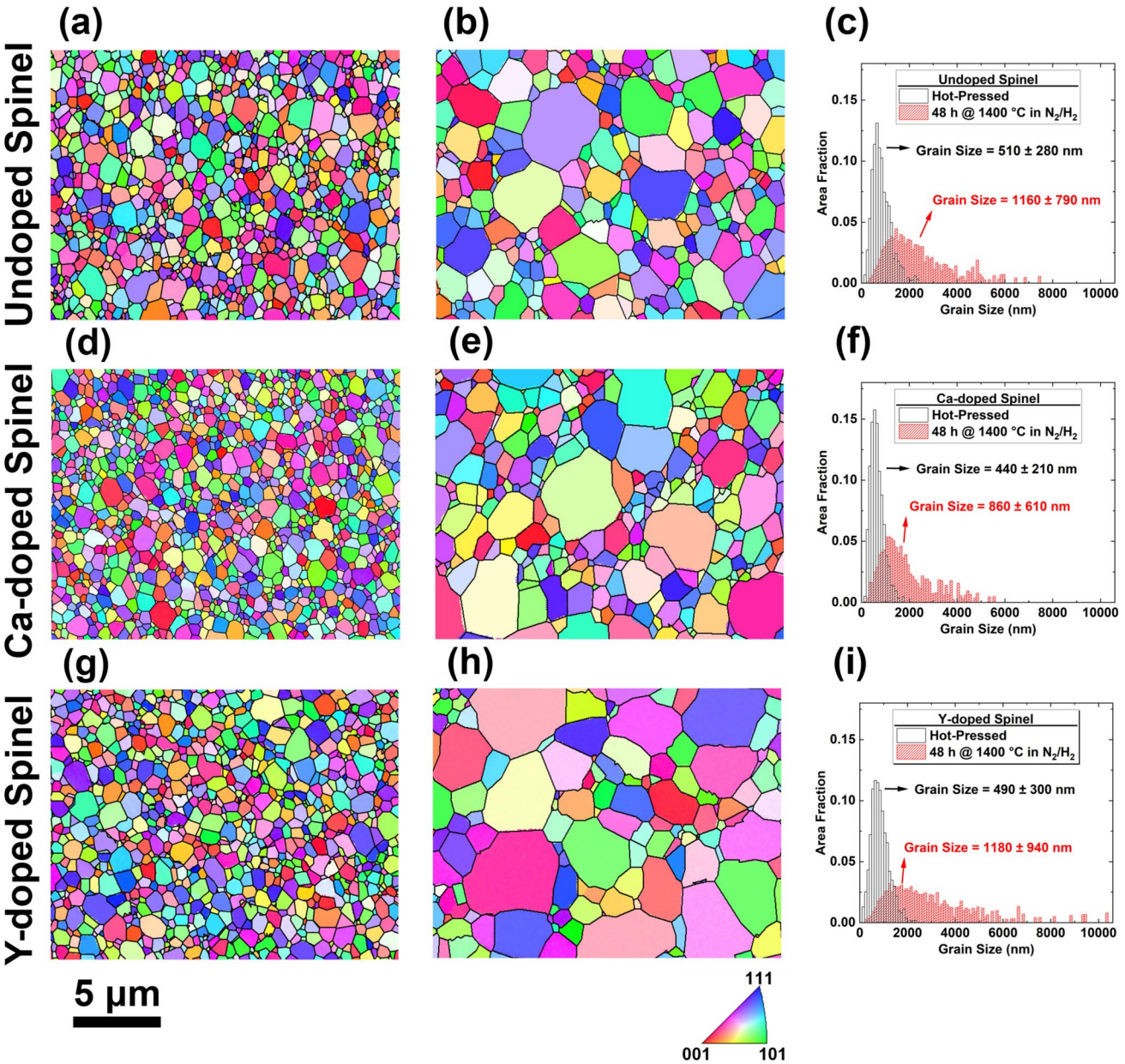

Figure 1 Results of EBSD analysis of undoped spinel **a** in the as-hot-pressed condition and **b** after annealing, Ca-doped spinel **d** in the as-hot-pressed condition and **e** after annealing and Y-doped spinel **g** in the as-hot-pressed condition and **h** after annealing. All annealing treatments were carried out at 1400 °C for 48 h in a N_2/H_2 atmosphere. The grain-size distributions for undoped, Ca-doped, and Y-doped spinel samples are compared in **c**, **f** and **i**, respectively. The dark solid lines in all the EBSD maps represent the reconstructed grain boundaries obtained from the OIM software. EBSD data for Ca-doped spinel in the as-hot-press condition extracted from [25].

(Fig. 1a, d and g). The average grain size after hot-pressing was ~ 510 nm for the undoped spinel, while the Ca- and Y-doped samples had an average grain size of ~ 440 nm and ~ 490 nm. After annealing treatments, the average grain size increased to ~ 1160 nm for the undoped sample, ~ 880 nm for the Ca-doped spinel, and ~ 1180 nm for the Y-doped spinel sample. For better visualization of the grain-size changes, the grain-size distributions for samples after hot-pressing and annealing treatments are shown in Fig. 1c, f and i. The grain-size measurements indicated that calcium doping resulted in a reduced grain growth

rate as compared to the undoped and Y-doped spinel samples. Although the average grain size in Y-doped spinel was nearly identical to undoped spinel some clusters of abnormally large grain were found after annealing as shown in Fig. 1S. The total area of the large grains was estimated to be < 5%. Due to the small fraction of these abnormally large grains, their effect on the segregation behavior and mechanical properties is considered negligible.

To obtain more detailed information from the EBSD results, the misorientation-angle distributions, grain-boundary plane distributions (GBPD), and grain-boundary character distributions (GBCD) were extracted using the stereological analysis developed by Saylor et al. [27, 28] from the EBSD results for the samples annealed at 1400 °C for 48 h. Figure 2a–c shows the misorientation-angle distributions for the undoped, Ca-doped and Y-doped spinel samples, respectively. All samples presented misorientation angles that mostly follow a random distribution. Only grain boundaries with misorientation angles between 36 and 38° in all samples and grain boundaries with misorientation angles ~ 45° in the Ca-doped sample occurred with a slightly higher frequency than a random distribution. Figure 2d–f presents the GBPDs irrespective of misorientation for the undoped and Ca- and Y-doped samples. The results indicate that all samples presented a tendency to have grain boundaries that terminate in {111} planes.

Figure 2g–i shows the GBCD for Σ3 coincident site lattice (CSL) grain boundary ($\lambda(\mathbf{n}|60°/[111])$) in undoped, Ca-doped, and Y-doped spinel samples, respectively. The Σ3 CSL grain boundary was selected for further analysis because it was the most frequent CSL grain boundary in the bulk. Also, the EBSD analysis indicated that for the misorientation angle of 60° the most frequent misorientation axis was the [111]. The positions of the pure twist boundary type and the pure tilt boundaries are indicated by a triangle and a white dashed line, respectively. The undoped spinel sample (Fig. 2g) presents a large GBCD anisotropy. Also, the maximum in the stereological projection appears at the (111) boundary plane (pure twist boundary with both crystals adjacent to the boundary terminating in (111) planes). It was observed that the grain boundaries with the pure twist configuration (triangle in Fig. 2g) were found ~ 6 times more frequently than expected in a random distribution. Conversely, tilt boundaries were found less frequently than expected in a random distribution as indicated by the broad purple band along the white dashed line in Fig. 2g (grain-boundary planes with multiples of random distribution (MRD) values below 1). After calcium and yttrium doping the anisotropy in the GBCD decreased. The maximum in the stereological projection remains at the position of the pure twist boundary but grain boundaries are only ~ 4 times more frequent than expected in a random distribution. On the other hand, the frequency of grain boundaries along the broad band corresponding to tilt boundaries increases after doping. A similar decrease in the GBCD anisotropy was found for all misorientation angles between 20° and 60° about the [111] directions as presented in Fig. 2S.

Calcium and yttrium segregation behavior at grain boundaries

HAADF-STEM imaging

To further characterize the segregation behavior of calcium and yttrium in spinel, detailed microstructure observations were performed at high resolution in an aberration-corrected STEM instrument. Figure 3 shows representative HAADF-STEM images of grain boundaries in near edge-on conditions in the undoped, Ca-doped, and Y-doped spinel samples after annealing. No impurities (besides calcium and yttrium) or secondary phases were found in any of the grain boundaries analyzed. It is worth noting that the intensity in HAADF-STEM imaging increases with the atomic numbers (Z), and therefore, this is a valuable technique to corroborate the presence of heavier dopant atoms at grain boundaries [38].

The Ca-doped spinel sample showed no enhanced intensity at the GB position (Fig. 3b). Direct observations of calcium atoms at grain boundaries in spinel are challenging due to the relatively low atomic number difference between calcium ($Z = 20$) and host atoms oxygen ($Z = 8$), magnesium ($Z = 12$) and aluminum ($Z = 13$) and the rather low amount of segregation. Therefore, spectrometry-based analysis of grain boundaries was necessary to confirm the segregation of calcium in spinel. In the case of the Y-doped spinel sample, the presence of yttrium at the grain boundary can be clearly discerned as enhanced intensity in Fig. 3c because of the high atomic number of yttrium ($Z = 39$). For this reason, a more detailed characterization of yttrium segregation behavior at the atomic scale was performed utilizing HAADF-STEM imaging

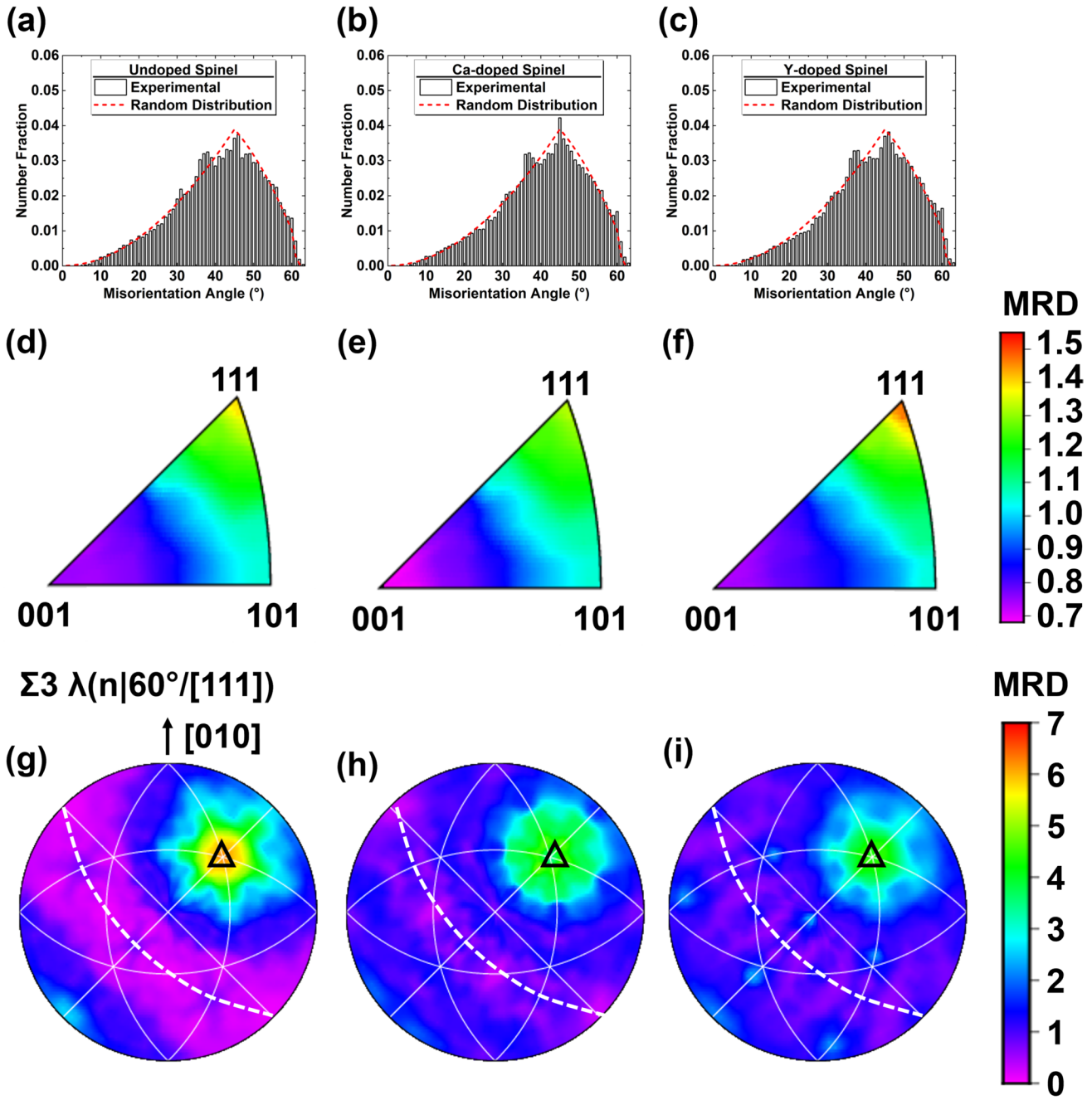

Figure 2 EBSD analysis of **a-c** misorientation angle, **d-f** grain-boundary plane distribution (GBPD) irrespective of misorientation, and **g-i** grain-boundary character distributions (GBCD) for the Σ3 λ(**n**|60°/[111]) coincident site lattice (CSL) grain boundary for undoped, Ca-doped and Y-doped spinel samples after annealing at 1400 °C for 48 h in N_2/H_2. The GBCD was plotted in stereographic projection along the [001] direction. The intensity in the GBPDs and GBCDs is expressed in multiples of random distribution (MRD). A triangle indicates the position of the pure twist boundary while a white dashed line indicates pure tilt boundaries.

to elucidate the exact position of yttrium atoms at grain boundaries in spinel.

Figure 4 shows direct observations by atomic-resolution HAADF-STEM imaging of yttrium atoms at grain boundaries in spinel. Figure 4a shows a grain boundary that was orientated to near edge-on condition. In this condition, the grains on both sides of the boundary were not aligned to any major zone axis.

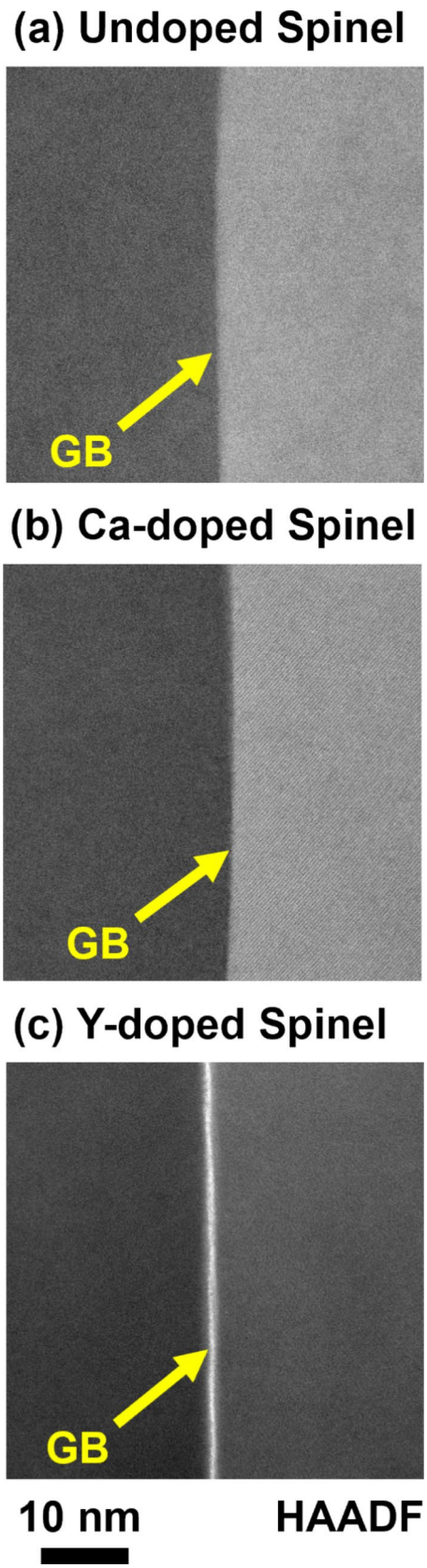

Figure 3 Representative high-angle annular dark-field scanning transmission electron microscopy (HAADF-STEM) images of grain boundaries in near edge-on conditions in the **a** undoped, **b** Ca-doped and **c** Y-doped spinel samples after annealing at 1400 °C for 48 h in N_2/H_2. Due to the atomic number difference between doping atoms and host cations, only the yttrium segregation at the grain boundary resulted in an enhanced intensity at the grain-boundary (GB) position.

However, some lattice planes can still be observed. Additionally, clear yttrium segregation was found as indicated by the enhanced intensity at the grain-boundary location. The full width a half maximum (FWHM) of this enhanced intensity region corresponding to yttrium segregation was ~ 0.6 nm. The exact location of yttrium atoms in the spinel structure cannot be determined from this edge-on configuration alone. For this reason, the grain on the bottom side of Fig. 4a was oriented along the [112] direction to have a clearer view of individual yttrium atom positions.

Figure 4b shows the atomic-scale HAADF-STEM image of the same grain boundary shown in Fig. 4a after tilting so that the [112] direction of the bottom grain is parallel to the electron beam. In this condition, only enhanced intensity at discrete locations of the grain boundary can be seen (red box in Fig. 4b), which corresponds to the positions of individual yttrium atoms. A magnified view of this region with enhanced intensity (Fig. 4c) revealed that yttrium atoms are separated by a distance of ~ 0.47 nm, which corresponds to the interplanar spacing of {111} planes. Also, Fig. 4d shows the position of the atoms in an ideal spinel structure oriented along the [112] direction drawn using the software VESTA [39]. The positions of yttrium atoms have been overlaid to the spinel structure at the grain boundary, revealing that yttrium atoms preferentially occupy aluminum octahedral sites.

Quantitative EELS analysis

Quantitative EELS analysis was performed in the undoped, Ca-doped and Y-doped spinel samples to gain more information about the spatial distribution of dopants and host cations in the vicinity of grain boundaries. As explained previously, direct observation of calcium atoms at grain boundaries in spinel

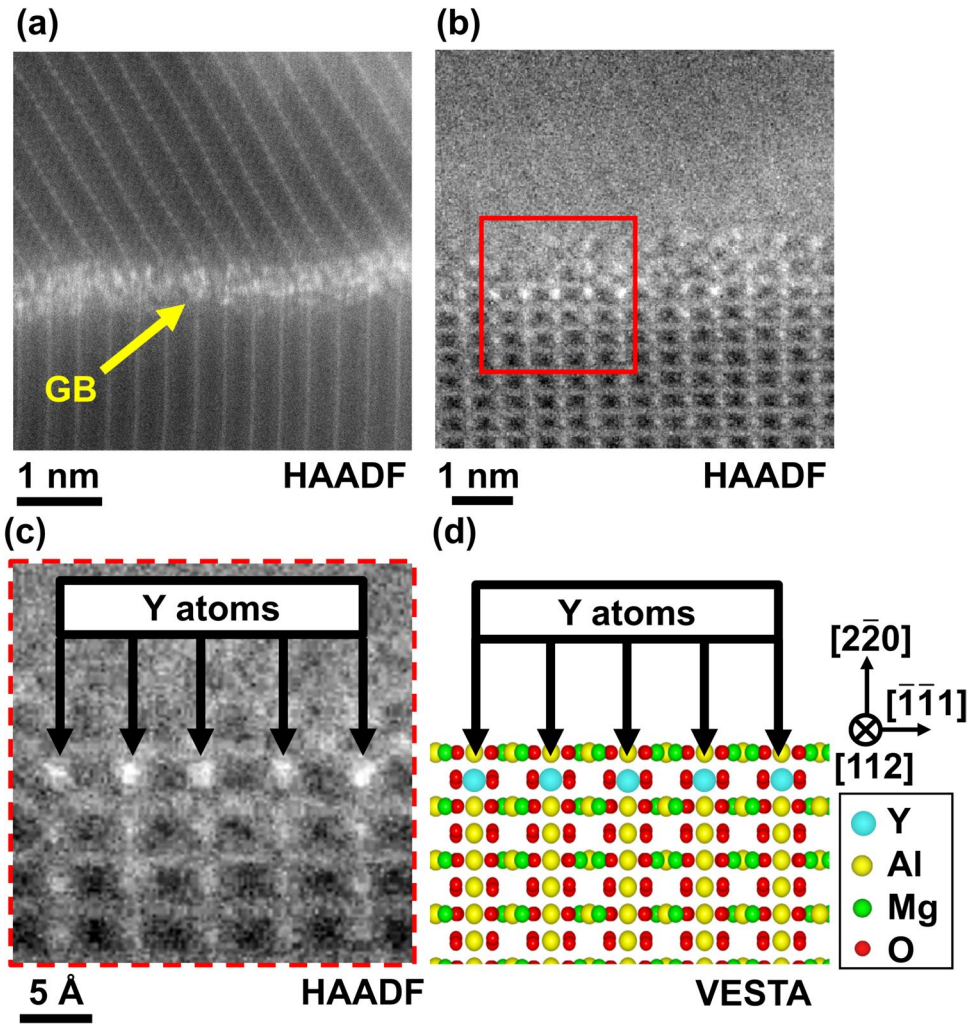

Figure 4 **a** Atomic-resolution high-angle annular dark-field scanning transmission electron microscopy (HAADF-STEM) image of a grain boundary in the Y-doped spinel sample after annealing at 1400 °C for 48 h in N_2/H_2 in near edge-on condition. **b** The same grain boundary in **a** but the grain on the bottom of the image was orientated along the [112] zone axis to facilitate the visualization of the yttrium segregation. **c** Detailed view of the area indicated by a red square in **b** showing the position of yttrium atoms at the grain boundary. **d** A schematic of the projected spinel structure in identical orientation as **c** drawn using the VESTA software [39]. Yttrium atoms preferentially occupy aluminum octahedral sites at the interface in this particular grain boundary.

by HAADF-STEM imaging is challenging due to the lower atomic number difference between dopant and host cations. For this reason, spectrometry analysis by EELS-SI was employed to study the segregation behavior of calcium in spinel. Special attention was paid to the effect of doping on the non-stoichiometry at the grain boundary.

EELS-SI datasets were acquired in the vicinity of grain boundaries in the undoped spinel sample and subsequent quantitative analysis was carried out to serve as a reference. Figure 5a shows the survey HAADF-STEM image, and Fig. 5b shows the HAADF-STEM image from the regions indicated by a red square in Fig. 5a acquired simultaneously with the EELS-SI dataset. Nanometer-scale facets were observed along the grain boundary as seen in Fig. 5b. Figure 5c shows the thickness of the analyzed area was below 0.5 t/λ indicating the probability of plural scattering was negligible. Hence, plural scattering deconvolution was not applied before the quantitative analysis. Figure 5d-f shows the quantitative maps corresponding to the Mg–K, Al-K and O-K edges, respectively. It is worth noting that a non-stoichiometric distribution of constituent atoms was found at the grain boundary. A magnesium depletion, coupled with aluminum excess and oxygen excess was observed in two different grain boundaries in undoped spinel investigated in this study.

Similarly, EELS quantitative analysis from the vicinity of a grain boundary in the Ca-doped spinel sample was performed. Figure 6a shows the survey HAADF-STEM image, and Fig. 6b shows the HAADF-STEM image from the regions indicated by a red square in Fig. 6a acquired simultaneously with the EELS-SI dataset. Relatively strong channeling contrast can be observed in the right-side grain in Fig. 6b.

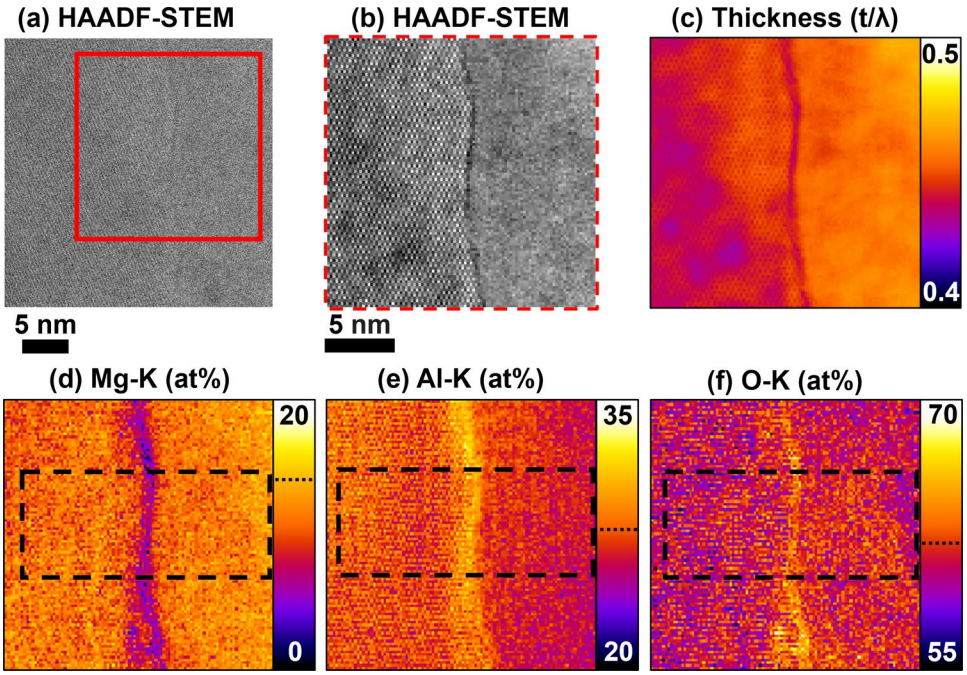

Figure 5 **a** A HAADF-STEM survey image used to determine the position of the area of interest for the EELS-SI dataset. **b** A HAADF-STEM image acquired simultaneously with an EELS-SI in the vicinity of a grain boundary in the undoped spinel after annealing at 1400 °C for 48 h in N_2/H_2. Quantitative maps corresponding to **c** relative specimen thickness and concentration corresponding to **d** the Mg–K, **e** Al-K, and **f** O-K ionization edges. The black dashed lines in the lookup table in **d**-**f** correspond to the composition of stoichiometric spinel (Mg: 14.3 at%, Al: 28.6 at%, and O: 57.1 at%).

Figure 6 **a** A HAADF-STEM survey image used to determine the position of the area of interest for the EELS-SI dataset. **b** A HAADF-STEM image acquired simultaneously with an EELS-SI in the vicinity of a grain boundary in the Ca-doped spinel after annealing at 1400 °C for 48 h in N_2/H_2. Quantitative maps corresponding to **c** relative specimen thickness and concentration corresponding to **d** the Ca-$L_{2,3}$, **e** Mg–K, **f** Al -K, and **g** O-K ionization edges. The black dashed lines in the lookup table in **e**–**g** correspond to the composition of stoichiometric spinel (Mg: 14.3 at%, Al: 28.6 at%, and O: 57.1 at%).

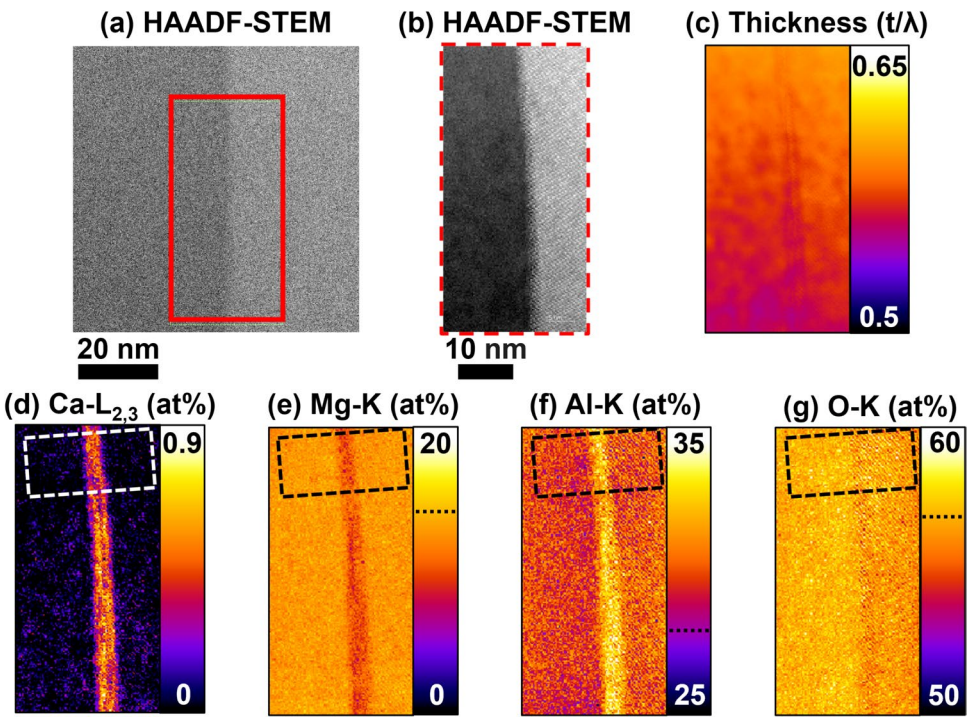

Additionally, the thickness of the analyzed regions was below 0.6 t/λ and therefore, plural scattering deconvolution was not applied to the EELS-SI dataset. Segregation of calcium (Fig. 6d) as well as magnesium depletion (Fig. 6e) and aluminum excess (Fig. 6f) can be clearly discerned at the grain boundary. Additionally, a slight oxygen depletion was found at the grain boundary as shown in Fig. 6g. This segregation behavior in Ca-doped spinel is consistent with EELS measurements taken in all three different grain boundaries analyzed in this study.

Similarly, EELS-SI datasets were acquired in the vicinity of grain boundaries in the Y-doped spinel sample. Figure 7a shows the HAADF-STEM survey image from the grain-boundary regions where a region of interest is indicated by a red square. Figure 7b shows the HAADF-STEM image from the area indicated in Fig. 7a. The thickness in Fig. 7c was below 0.6 t/λ, and therefore, no plural scattering devolution was applied to the EELS-SI dataset. Figure 7d shows clear segregation corresponding to yttrium at the grain boundary. Magnesium depletion at the grain boundaries was also found in this sample (Fig. 7e). A more complex aluminum distribution was observed at the grain boundary compared to the undoped and Ca-doped conditions (Fig. 7f). The grain-boundary core was depleted of aluminum while the neighboring area was enriched in aluminum. Also, oxygen depletion was found at the grain-boundary core as illustrated in Fig. 7g. Here it is worth noting that this segregation behavior was discernable in all 3 different grain boundaries analyzed in this study and it is only noticeable when the grain boundary is almost perfectly aligned to the edge-on condition. For example, the bottom region in Fig. 7d presents yttrium segregation but no clear aluminum excess with depletion in the grain-boundary core was seen because the grain-boundary orientation locally changed in this area, leaving the grain boundary slightly away from the edge-on condition.

To better visualize and compared the differences in the segregation behavior between the undoped and the Ca- and Y-doped spinel samples, line profiles were extracted from the dotted rectangular regions in Figs. 5, 6 and 7 for the magnesium, aluminum, oxygen, calcium and yttrium concentrations. Figure 8a shows magnesium depletion as well as aluminum and oxygen excess at the grain-boundary position in the undoped spinel sample. Figure 8b shows the calcium segregation,

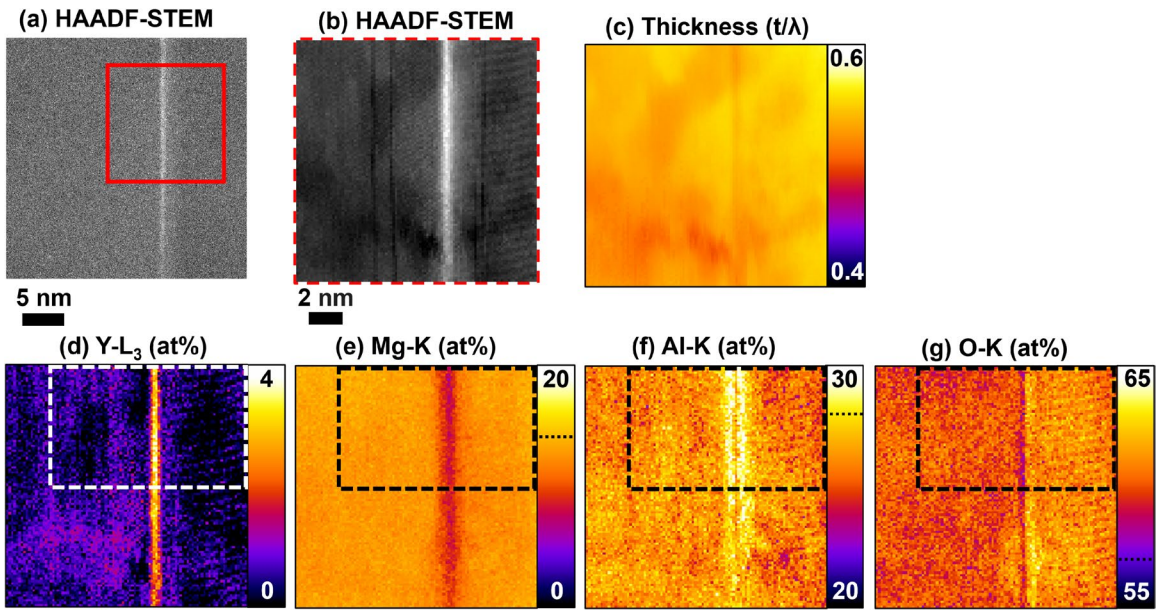

Figure 7 **a** A HAADF-STEM survey image used to determine the position of the area of interest for the EELS-SI dataset. **b** A HAADF-STEM image acquired simultaneously with an EELS-SI in the vicinity of a grain boundary in the Y-doped spinel after annealing at 1400 °C for 48 h in N_2/H_2. Quantitative maps corresponding to **c** relative specimen thickness and concentration corresponding to **d** the Y-L_3, **e** Mg–K, **f** Al -K, and **g** O-K ionization edges. The black dashed lines in the lookup table in (e–g) correspond to the composition of stoichiometric spinel (Mg: 14.3 at%, Al: 28.6 at%, and O: 57.1 at%).

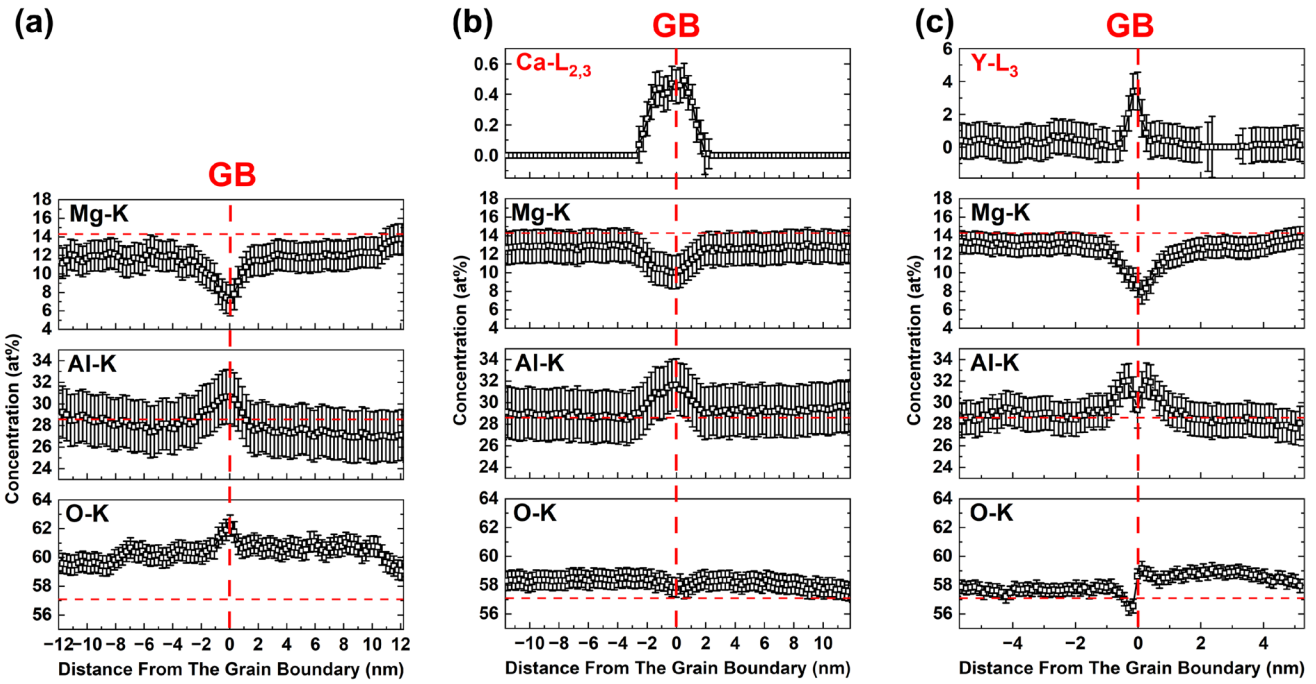

Figure 8 Concentration profiles of constituent atoms in spinel as extracted from the box regions indicated in Figs. 5–7 for **a** undoped spinel, **b** Ca-doped spinel and **c** Y-doped spinel samples after annealing at 1400 °C for 48 h in N_2/H_2. The error bars represent a 99% confidence limit ($\pm 3\sigma$), and the horizontal dashed lines correspond to the stoichiometry composition of spinel (Mg: 14.3 at%, Al: 28.6 at%, and O: 57.1 at%).

magnesium depletion, aluminum excess, and slight oxygen depletion in the Ca-doped spinel sample. Figure 8c presents the concentration profiles for the Y-doped sample. Yttrium segregation at the core of the grain boundary is clearly discernible. Moreover, the grain boundaries were deficient in both magnesium and oxygen as compared to bulk after yttrium doping. A unique aluminum segregation behavior characterized as a "V" shape around the core of the boundary was observed. The core of the boundary was depleted of aluminum along with an excess of aluminum atoms just off the grain-boundary core region into the grains on both sides of the boundary.

It is worth noting that the calcium segregation appears to be broader compared to the yttrium segregation. The calcium segregation peak in Fig. 8b presented a FWHM of ~ 3 nm while the yttrium segregation peak in Fig. 8c was ~ 0.5 nm. This broader calcium segregation occurred because the grain boundary was inclined during the EELS-SI acquisition. As the calcium segregation cannot be readily observed in HAADF-STEM imaging, it is difficult to orient the grain boundaries close to the edge-on condition compared to Y-doped spinel sample.

Quantitative XEDS analysis

Although the EELS results provided information about the segregation of host and dopant atoms with sub-nanometer spatial resolution in the grain-boundary vicinity, it is not possible to determine the deviation (excess or depletion) of the constituents and dopants at the grain boundary effectively from the EELS results. Hence, quantitative XEDS analysis using the ζ-factor method was carried out in the vicinity of several grain boundaries. The acquisition of the XEDS spectra was carried out as a function of the grain-boundary misorientation angle. TKD analysis on the SEM was used to determine the misorientation angle of all grain boundaries on the thin TEM lamella. Then, low- and high-angle grain boundaries were selected

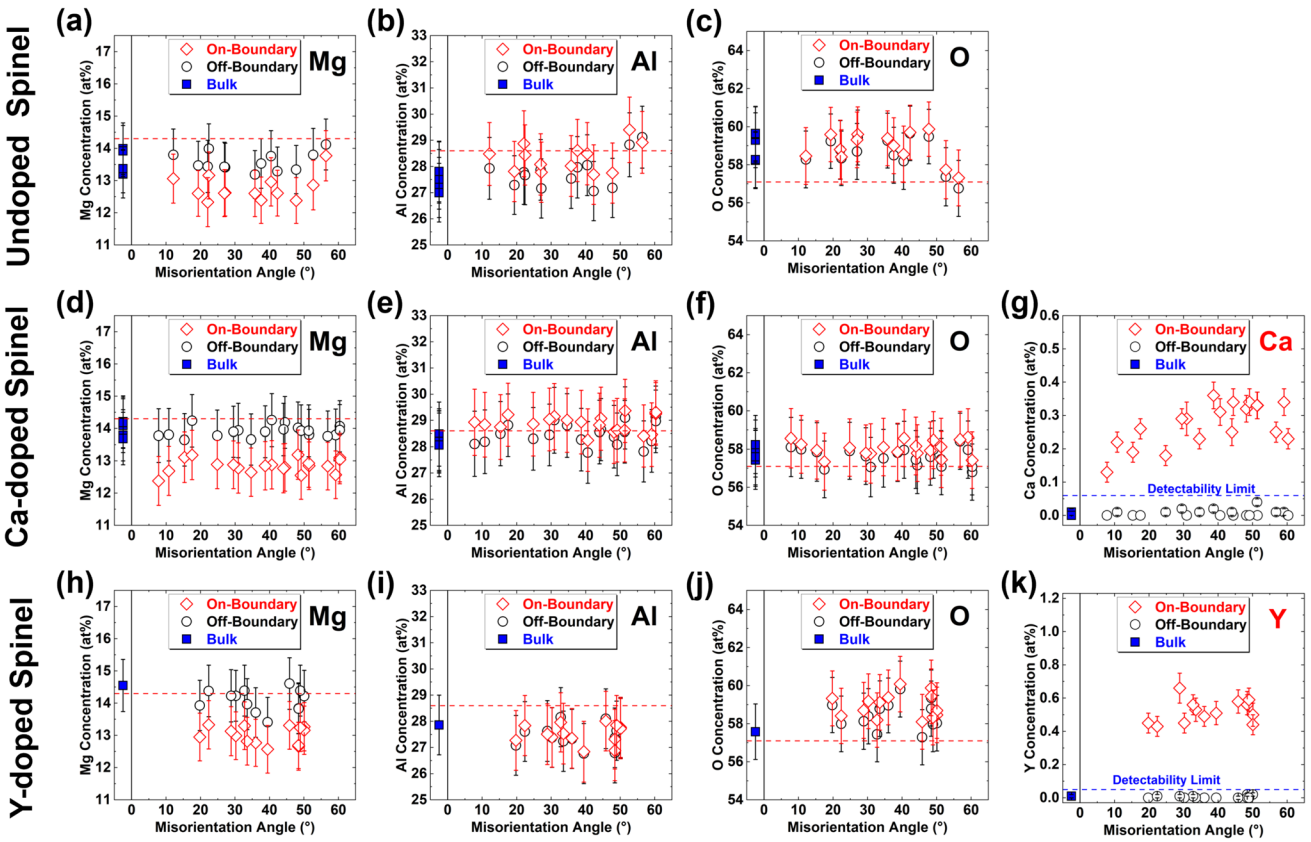

Figure 9 Quantitative XEDS analysis using the ζ-factor method in the vicinity of different grain boundaries, plotted as a function of misorientation angle. The concentration of **a** magnesium, **b** aluminum and **c** oxygen in undoped spinel, **d** magnesium, **e** aluminum, **f** oxygen and **g** calcium in Ca-doped spinel and **h** magnesium, **i** aluminum, **j** oxygen and **k** yttrium in Y-doped spinel samples after annealing at 1400 °C for 48 h in N_2/H_2. The red horizontal dashed lines in **a**-**c**, **d**-**f** and **h**-**j** represent the stoichiometry composition of spinel (Mg: 14.3 at%, Al: 28.6 at%, and O: 57.1 at%) and the error bars represent a 99% confidence limit ($\pm 3\sigma$). The detectability limit for calcium and yttrium was ~ 0.03 ± 0.01 at% and ~ 0.04 ± 0.02 at%, respectively, estimated from the fluctuation of background intensities under the Ca-K and Y-K peaks based on the criterion for a minimum detectable peak ($I > 3\sqrt{2B}$, where I is the peak intensity above the background intensity B [42]) .

for the XEDS analysis with the aim of covering a wide range of different grain-boundary types.

Figure 9 shows the concentration of magnesium, aluminum and oxygen for the undoped, Ca-doped and Y-doped spinel samples as well as the concentration of calcium and yttrium on-boundary, off-boundary and in the bulk positions. Remarkably good agreement with the quantitative EELS analysis was found in the case of magnesium concentration (Fig. 9a, d and h) where all samples presented magnesium depletion at the on-boundary position compared to the off-boundary (~ 28 nm away from the grain boundary) and the bulk (several hundreds of nanometers away from the grain boundary). Additionally, aluminum excess at the boundary position was found in the undoped and Ca-doped spinel samples but no significant change in the case of the Y-doped spinel sample (Fig. 9b, e and i). Here it is worth noting that, for the XEDS analysis, the box method was used consisting of scanning the beam over an area of approximately ~ 12×75 nm^2 and therefore subtle details in the segregation behavior such as the "V" shape segregation behavior obtained by EELS-SI were missed. In other words, the aluminum concentration at the boundary position for the Y-doped spinel samples was averaged out in the XEDS analysis due to the size of the scanned area, resulting in a net zero change in the composition compared to the off-boundary position. In the case of the oxygen concentration (Fig. 9c, f and j), the on-boundary position presented slightly higher concentration than the off-boundary and bulk positions in the undoped Ca-doped or Y-doped spinel samples.

Finally, the calcium and yttrium concentrations are shown in Fig. 9g and k, respectively. The calcium concentration ranged from ~ 0.1–0.4 at% while the yttrium concentration was between ~ 0.4–0.7 at%. A higher calcium concentration at grain boundaries with high angles of misorientation was observed. On the other hand, there is no strong correlation between the yttrium concentration and the grain-boundary misorientation angle. No calcium or yttrium was found in the off-boundary or bulk positions considering the minimum detectability limit of the XEDS analysis employed (~ 0.03 ± 0.01 at% and ~ 0.04 ± 0.02 at%, respectively, and the errors indicate the 3σ ranges). These measurements are consistent with previous studies that considered the solubility of calcium and yttrium in spinel negligible or below the detectability limit of the different analyses utilized [40, 41].

A more thorough measurement of the segregation behavior of calcium, yttrium and host cations aluminum and magnesium was performed deconvoluting the boundary inclination, beam-broadening and thickness effects. The XEDS measurements were quantified

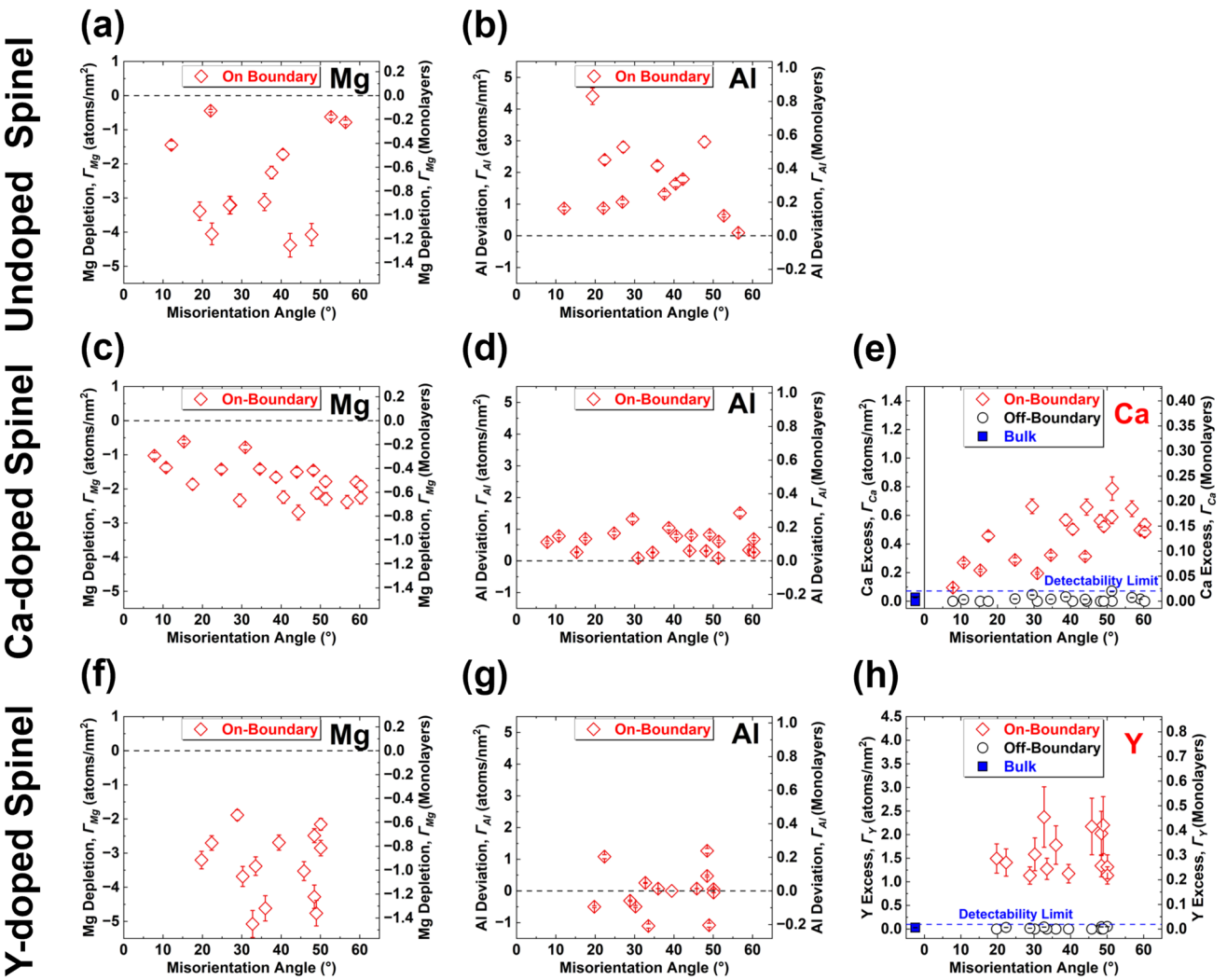

Figure 10 Elemental deviations of magnesium and aluminum at grain boundaries in **a**-**b** undoped, **c**-**d** Ca-doped and **f**-**g** Y-doped spinel samples after annealing at 1400 °C for 48 h in N_2/H_2, respectively. Calcium and yttrium excess are shown in **e** and **h**, respectively. The error bars represent a 99% confidence limit (±3σ). The detectability limit of calcium and yttrium was ~ 0.03 ± 0.01 at% (0.07 ± 0.02 atoms/nm^2) and ~ 0.04 ± 0.02 at% (0.11 ± 0.06) atoms/nm^2), respectively, estimated from the fluctuation of background intensities under the Ca-K and Y-K peaks based on the criterium for a minimum detectable peak ($I > 3\sqrt{2B}$, where I is the peak intensity above the background B [42].

in terms of grain-boundary excess or depletion and thus, the results can be readily compared with other such measurements.

Figure 10 shows the elemental deviations of magnesium and aluminum at grain boundaries in undoped, Ca-doped and Y-doped spinel as well as the calcium and yttrium excess, calculated using Eq. (1). Here, the number of monolayers was calculated assuming a (111) plane since this was the most frequent grain-boundary plane as shown in Fig. 2. In the undoped spinel (Fig. 10a and b), the magnesium depletion was quantified in the range of ~ 0.5–4.5 atoms/nm^2 (~ 0.2–1.3 monolayers), while the aluminum excess was in the range from ~ 0–4.5 atoms/nm^2 (~ 0–0.8 monolayers). Here it is worth noting that the magnesium depletion and aluminum excess might be distributed over more than one monolayer in the vicinity of the grain boundary due to the formation of a space-charge layer with a width of a few nanometers [18, 43–45]. Line scans shown in Fig. 8 indicated that for grain boundaries near edge-on conditions, the main features of the non-stoichiometry are restricted to a width of < 6 nm. Therefore, the raster-scan box used in the XEDS analysis with a width of ~ 12 nm is considered to include the vast majority of the localized changes in composition at the grain boundaries.

For the Ca-doped spinel sample, the magnesium depletion was ~ 0.5–2.5 atoms/nm^2 (~ 0.2–0.8 monolayers) and the aluminum excess was ~ 0.1–1.5 atoms/nm^2 (~ 0.02–0.3 monolayers). It has been previously demonstrated by the research group that calcium preferentially substitutes magnesium at grain boundaries in Ca-doped spinel [25]. For this reason, the calculation of calcium excess was performed assuming calcium simply replaces magnesium at the grain boundary, given an excess of ~ 0.1–0.8 atoms/nm^2 (~ 0.03–0.23 monolayers).

In the case of Y-doped spinel, the magnesium depletion was in the range of ~ 0.2–0.5 atoms/nm^2 (~ 0.5–1.5 monolayers). The aluminum deviation ranged from an excess of ~ 1.3 atoms/nm^2 (~ 0.25 monolayers) to a depletion of ~ 1.1 atoms/nm^2 (~ 0.2 monolayers). On average, the aluminum deviation in the Y-doped specimen was ~ 0 atoms/nm^2, accounting for the depletion at the boundary core and the excess in the surrounding area. Direct observations by HAADF-STEM imaging (Fig. 4) and quantitative EELS mapping (Fig. 7) indicated that yttrium preferentially occupies aluminum sites at the grain-boundary position. Therefore, for the calculation of yttrium excess, it was assumed that yttrium simply replaces aluminum. In that case, the yttrium excess was in the range of ~ 1.1–2.4 atoms/nm^2 (~ 0.2–0.45 monolayers).

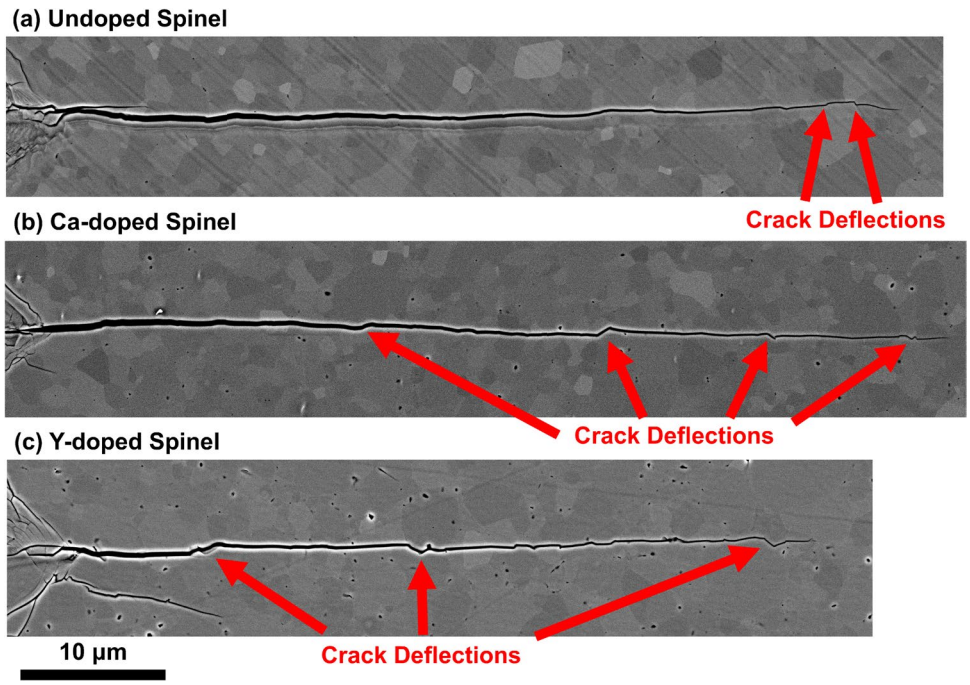

Figure 11 Representative SEM images of cracks introduced by Vickers microhardness indentations in **a** undoped, **b** Ca-doped and **c** Y-doped spinel samples after annealing at 1400 °C for 48 h in N_2/H_2. More significant crack deflections (more tortuous path) can be observed in the Ca- and Y-doped spinel samples compared to the undoped condition.

Bulk mechanical properties and fracture behavior

The fracture behavior of the spinel samples was investigated by analyzing the cracks induced by Vickers indentation. SEM micrographs of a set of representative cracks for the undoped, Ca-doped and Y-doped spinel are presented in Fig. 11. The crack propagated from left to right in the image for all the cracks presented in Fig. 11. A small section of the Vickers indentation mark can be seen on the left side of the SEM images in Fig. 11. The cracks primarily emanated from the 4 corners of the residual Vickers indentation marks, but secondary cracks were also observed. Figure 11a shows a representative crack in the undoped spinel sample where the crack path is primarily straight with minor crack deflections near the crack tip as indicated by red arrows. In the case of Ca-doped spinel (Fig. 11b), more crack deflections can be seen along the crack path. For the Y-doped spinel sample (Fig. 11c), more pronounced crack deflections (more tortuous path) can be seen as indicated by arrows. The average crack length for the undoped spinel was 77.8 ± 1.1 μm, which decreased to 74.1 ± 1.1 μm for Ca-doped spinel and further decreased to 73.6 ± 1.0 μm for Y-doped spinel (error corresponding to a 99% confidence level). Despite some electron channeling contrast that allows visualizing some of the grains along the crack trajectory, it is not easy to differentiate between regions of the crack with transgranular or intergranular fracture. For this reason, EBSD analysis in the vicinity of the cracks was carried out to obtain a better insight into the crack propagation behavior.

Figure 12 shows the results of SEM/EBSD analyses performed in the vicinity of cracks for the undoped, Ca-doped and Y-doped spinel samples. For this

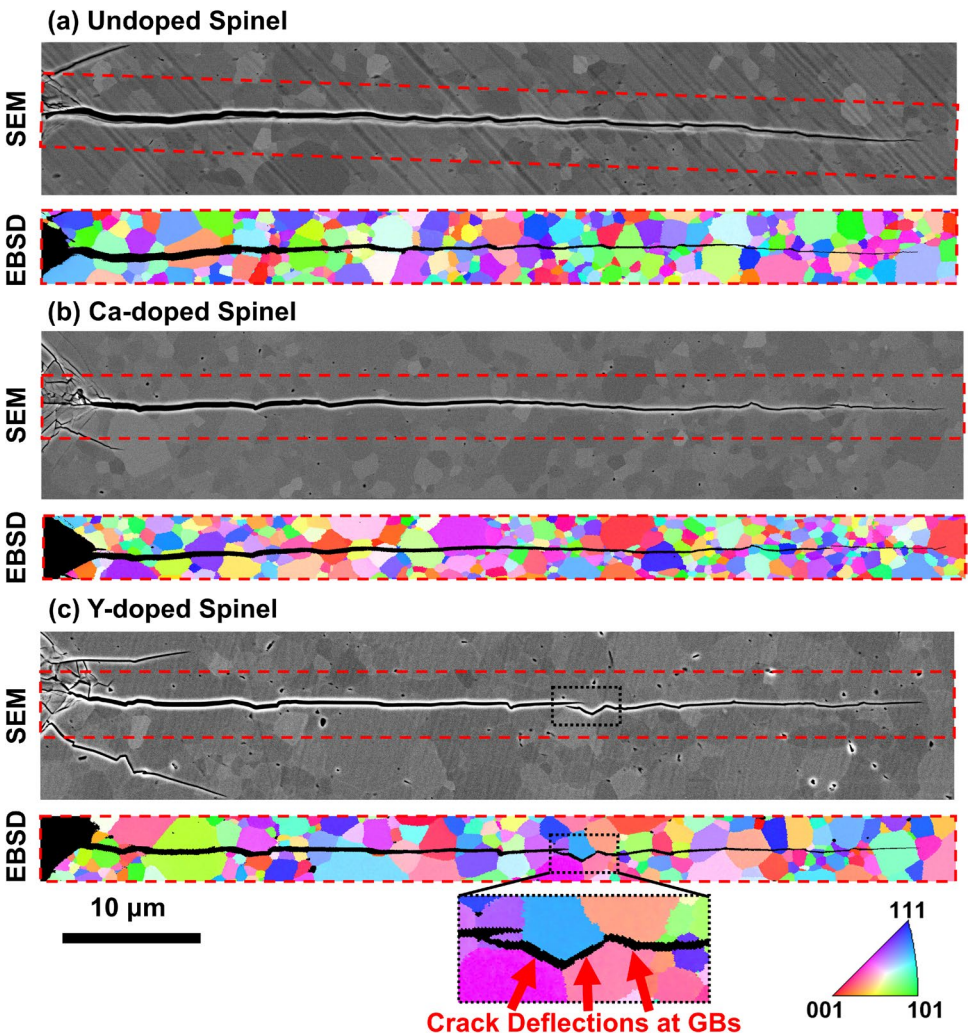

Figure 12 Sets of SEM image (top) and a corresponding EBSD map (bottom) for **a** undoped, **b** Ca-doped and **c** Y-doped spinel showing crack propagation behaviors after annealing at 1400 °C for 48 h in N_2/H_2. The magnified view in **c** shows a region of the crack where consecutive crack deflections at the grain boundaries occurred.

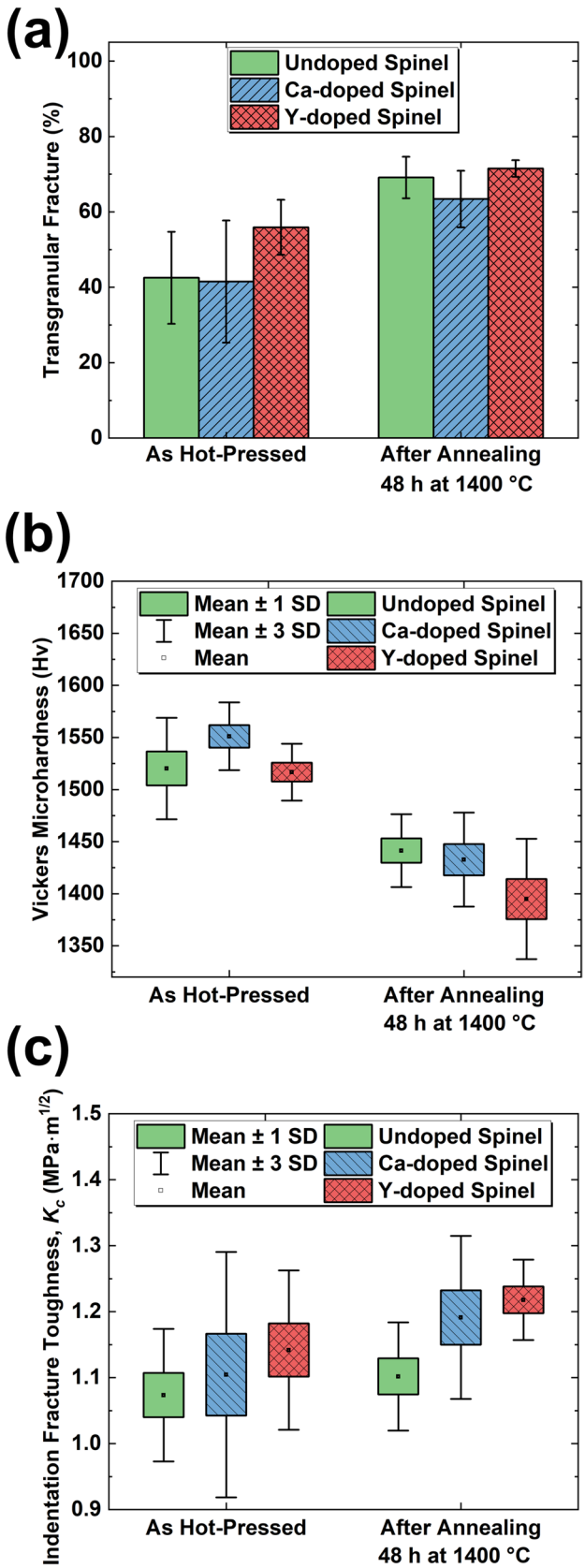

Figure 13 Summary of mechanical properties measurements showing **a** percentage of transgranular fracture, **b** Vickers microhardness and **c** indentation fracture toughness for undoped, Ca-doped and Y-doped spinel in the as-hot-pressed and after annealing conditions. Mechanical properties for Ca-doped spinel in the as-hot-press condition extracted from [25].

analysis, cracks with spallation were excluded. The EBSD analysis revealed that the fracture behavior for all samples was a mixture of intergranular and transgranular cracking. The Y-doped spinel sample presented evidence of crack bridging, as seen in the SEM image of Fig. 12c (dotted black box). A magnified view of the same region but in the EBSD analysis of Fig. 12c shows how this crack bridging is followed by intergranular cracking and more significant changes in the crack trajectory occurred when the crack was deflected by the grain boundaries. However, some minor crack deflections also occurred at grain boundaries between two adjacent grains with transgranular fractures (Fig. 3S). Additionally, the Y-doped spinel sample presented more secondary cracks emanating from the corners of the indentation marks than undoped and Ca-doped spinel.

Figure 13 shows the summary of the mechanical properties of all the samples in the as-hot-pressed and after annealing. First, Fig. 13a shows the percentage of the total crack length corresponding to transgranular grains. The fraction of transgranular cracking was determined by measuring the length of grains with the same orientation (same color in the IPF maps) on both sides of the crack normalized by the total length of the crack using EBSD analysis. The indentation cracks propagated transgranularly for 40% to 55% of the crack length in the as-hot-pressed undoped and doped samples. After annealing, the transgranular fracture increased, being very similar for undoped (69.1 ± 5.5%) and Y-doped spinel (71.5 ± 2.2%) and slightly lower for Ca-doped spinel (63.4 ± 7.5%) (error bars corresponding to a 95% confidence level). The Vickers microhardness results (Fig. 13b) indicated that the microhardness decreased after annealing for all samples. Figure 13c shows that the indentation fracture toughness of the Ca- and Y-doped samples increased after annealing. Additionally, the fracture toughness of the Ca- and Y-doped samples is higher than in the undoped conditions, especially after annealing (Fig. 13c).

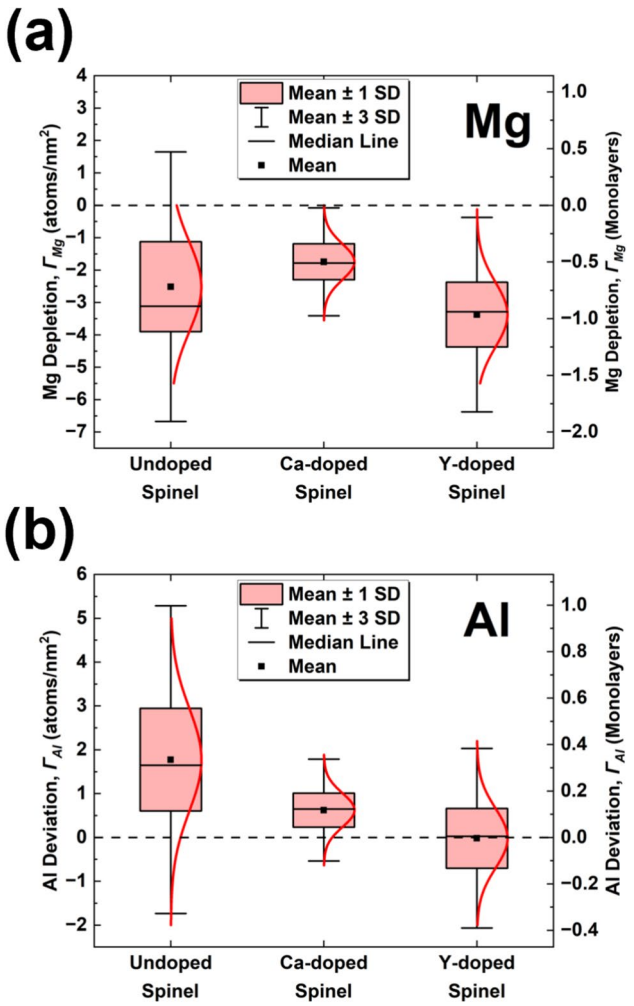

Figure 14 Summary of elemental deviations (excess or depletion) of **a** magnesium and **b** aluminum at grain boundaries in undoped, Ca-doped, and Y-doped spinel after annealing at 1400 °C for 48 h in N_2/H_2.

Discussion

Calcium and yttrium segregations at grain boundaries in spinel were confirmed by EELS and XEDS analysis of individual grain boundaries. No secondary phases, additional impurities or intergranular films were detected in any of the grain boundaries analyzed in this study. Thus, the changes in the grain-boundary character distribution, the impact on the fracture behavior and the increase in indentation fracture toughness can be considered primarily due to the segregation of calcium and yttrium atoms at the grain boundaries. This isolated effect of segregation provides a key opportunity to thoroughly discuss new insights into how grain-boundary segregation, a phenomenon at the nanoscale, affects the mechanical properties at the microscale in spinel, as detailed below.

Effect of calcium and yttrium segregation on the grain-boundary character distribution

Figure 1 shows that calcium doping reduced the grain growth rate compared to undoped spinel. Similar grain growth suppression has been observed in Ca-doped spinel samples where smaller grain sizes compared to undoped spinel can be explained as a solute drag effect [20, 25]. Yttrium doping had no significant effect on the average grain size compared to undoped spinel. This is in good agreement with a previous study by Zubrzycka and coworkers where the crystallite size was very similar with and without yttrium doping [46]. A systematic study involving heat treatments at different temperature/time conditions could provide clearer insight into the effect of calcium and yttrium segregation on grain growth behavior. This research was focused on the grain-boundary segregation behavior of calcium and yttrium and their effect on microhardness, fracture toughness and crack propagation behavior. Hence a study of grain growth effects was not pursued.

Figure 1 shows that no significant grain-orientation texture was found in the EBSD analysis for any of the samples, irrespective of doping condition or annealing treatment. Also, Fig. 2(d–f) shows that calcium and yttrium segregation at grain boundaries had no significant impact on the GBPD irrespective of misorientation. It was found that all samples after annealing tended to form grain boundaries terminating in {111} planes. However, calcium and yttrium segregations in spinel grain boundaries had a great impact on the GBCD, as shown in Fig. 2(g–i). Over a wide range of misorientation angles about the [111] axis (from 20 to 60°), two main trends were identified. Ca- and Y-doped spinel samples presented a higher frequency of tilt boundaries, and a lower frequency of pure twist boundaries, compared to undoped spinel.

It could be argued that the free volume available in the twist and tilt boundaries and the ability to accommodate the larger dopant atoms within these

spaces is the key driving force for the changes in the GBCDs. Pure tilt boundaries are exclusively formed by edge dislocations while pure twist boundaries are formed by screw dislocations [47]. Edge dislocations have larger excess free volumes compared to screw dislocations [48]. The most thermodynamically stable configuration for the larger yttrium and calcium cations in spinel grain boundaries is where the elastic strain is minimal. The larger excess free volume at tilt boundaries compared to twist boundaries facilitates the accommodation of larger yttrium (r_i = 90 pm [16]) and calcium (r_i = 100 pm [16]) cations at grain boundaries in spinel. Therefore, dopants can induce the formation of more tilt boundaries as compared to twist boundaries to minimize the elastic strain energy at the interface. Thus, the prevalence of the tilt boundaries in the annealed doped samples was considered to be a result of energy minimization during annealing due to calcium and yttrium segregation.

During annealing, calcium and yttrium promote the formation of tilt boundaries as the grain-boundary energy of those boundaries is expected to decrease after segregation. Consequently, the area fraction of tilt boundaries grows allowing the accommodation of even more excess dopants, at the expense of less energetically favorable twist boundaries that can accommodate far less excess dopant. The changes in the population of grain boundaries with the [111] rotation axis occurred over a wide range of misorientation angles. However, the reason why this phenomenon is accentuated in the $\lambda(\mathbf{n}|60°/[111])$ population of grain boundaries is because of the highly symmetric Σ3 CSL grain boundary. The symmetry of the Σ3 grain boundary is such that the atoms at the interface occupy positions where the first nearest neighbors resemble those in the bulk, allowing almost no free space for segregation to occur [49].

The overall effect of the calcium and yttrium segregation on the population of grain boundaries with the [111] rotation axis is that the boundary anisotropy was considerably reduced. An inverse correlation between the frequency of grain boundaries in a specific population and the grain-boundary energy has been found by Saylor et al. [50]. Therefore, it is reasonable to expect that the grain-boundary energy anisotropy was also reduced after calcium and yttrium doping compared to undoped spinel for grain boundaries with the [111] rotation axis.

Segregation behavior of calcium and yttrium atoms in spinel

All grain boundaries analyzed in this study for the Ca- and Y-doped spinel samples presented segregation of the corresponding dopants. There is an important component of the segregation driving force arising from the elastic strain due to the ionic size mismatch between dopants and host cations [51]. The ionic radii of the dopant cations are 100 pm for Ca^{2+} and 90 pm for Y^{3+}, compared to 57 pm for Mg^{2+} in tetrahedral sites and 53 pm for Al^{3+} in octahedral sites. [16]. Therefore, this ionic radius mismatch, together with a reduction of the grain-boundary energy [52], contributed to the grain-boundary segregation of calcium and yttrium in spinel.

All the spinels, doped and undoped, exhibited non-stoichiometry of cations at the grain boundary. For undoped spinel, a depletion of magnesium and excess aluminum (Mg:Al ratio < 1) was observed. This is consistent with previous studies where magnesium depletion and aluminum excess were found at the grain boundaries [44, 53]. Therefore, the segregation behavior for the undoped spinel was used as a reference point for the discussion of calcium and yttrium segregation behaviors. Additionally, the discussion of the segregation behavior will be mainly focused on the changes in the cation sublattices, leaving aside the oxygen sublattice, since calcium and yttrium are expected to either occupy magnesium or aluminum sites at the grain boundary.

There are only a handful of previous studies in spinel where the exact position of dopant atoms at grain boundaries has been determined. For instance, in Eu-doped spinel, there is a tendency of europium to occupy aluminum sites in spinel [15, 17]. Another case is Yb-doped spinel where ytterbium forms staggered pairs at the grain boundary occupying both magnesium tetrahedral and aluminum octahedral sites [8]. These two dopant elements have different effects on the grain-boundary fracture toughness and therefore it is of great interest to determine the exact position of calcium and yttrium atoms at grain boundaries to have a better understanding of their effects on the mechanical properties.

In the case of Y-doped spinel, Y^{3+} preferentially occupies Al^{3+} octahedral sites at grain boundaries in

spinel as can be directly seen by HAADF-STEM imaging (Fig. 4). Quantitative analysis by EELS-SI (Fig. 5) revealed that there was preferential aluminum segregation at grain boundaries in the undoped spinel sample after annealing at 1400 °C for 48 h in N_2/H_2. Hence, it is reasonable to expect competition at the grain-boundary core between segregating Y^{3+} cations and host Al^{3+} cations. This grain-boundary segregation competition is exemplified in Fig. 7, where the segregation of yttrium at grain boundaries causes aluminum atoms to migrate away from the grain-boundary core. The migration of aluminum away from the boundary is reasonable considering the large ionic radius of Y^{3+} cations, making the incorporation of yttrium in the lattice thermodynamically unstable due to the large elastic strain.

In the case of Ca-doped spinel, direct observation of calcium atoms by HAADF-STEM imaging was not very straightforward due to the relatively lower atomic number difference between calcium and host cations. Instead, EELS-SI results indicated that calcium segregation at grain boundaries occurred. Additionally, magnesium depletion and aluminum excess at the grain boundary were present, similar to the undoped spinel. This segregation behavior is also consistent with previous studies on Ca-doped spinel [18]. Regarding the position of the calcium atoms at the grain boundaries, calcium atoms occupying aluminum sites would introduce additional elastic strain to the grain boundary since aluminum is already found in excess. Therefore, the most plausible option is that calcium simply replaces magnesium atoms at the boundary. A similar conclusion has been drawn in a previous study on Ca-doped spinel annealed at 1400 °C for 48 h in an air atmosphere [25].

The calcium excess presented a tendency to increase with the misorientation angle, while the yttrium excess remained almost constant. The reason for the anisotropy in the grain-boundary segregation of calcium could be related to the larger ionic radius of calcium (100 pm [16]) compared to yttrium (90 pm [16]). Calcium can be more easily accommodated at high-angle grain boundaries where, in general, more excess free volume is available for segregation. Yttrium, with a smaller ionic radius, can more easily fit at the grain boundaries of all misorientation angles. However, a larger number of grain boundaries analyzed by XEDS are necessary to draw clearer conclusive trends between the ionic radius and the anisotropy in the grain-boundary segregation in spinel.

The quantitative XEDS results were in very good agreement with the EELS-SI analysis. The non-stoichiometry at grain boundaries was quantified in terms of elemental deviations, either depletion or excess at the grain boundaries, not only for the dopant atoms but also for host cations (Fig. 10). To summarize the results from Fig. 10, the average values of elemental deviations for magnesium and aluminum at grain boundaries in undoped, Ca-doped and Y-doped spinel are shown in Fig. 14. Ca-doped spinel was characterized by a slight decrease in the magnesium depletion and the aluminum excess compared to the undoped spinel. Y-doped spinel had a more significant reduction in the aluminum excess compared to Ca-doped spinel, as shown in Fig. 14. The analysis of elemental deviation in this study evidence how segregation of dopants at grain boundaries in spinel affects the local composition of host cations, modifying the non-stoichiometry at the interfaces.

Effect of calcium and yttrium doping on the mechanical properties in spinel

It is worth noting that all samples presented very similar porosity levels. Also, previous studies have found that changes in grain size of up to ~ 30 μm (much greater than grain-size differences in this study of only ~ 300 nm) had no significant effect on the fracture toughness measurements of spinel [54]. As the porosity and grain-size differences being ruled out, the main discussion will be focused on the differences in the segregation behavior of calcium and yttrium compared to undoped spinel and their effect on the mechanical properties. Figure 2 shows that calcium and yttrium doping increase the fraction of tilt boundaries compared to undoped spinel. However, to determine whether tilt boundaries have higher fracture toughness compared to twist boundaries and potentially increase the bulk fracture toughness or not, micromechanical testing of individual grain boundaries is essential.

Crack deflections appeared to be more prominent in the Ca-doped spinel sample compared to the undoped spinel, and even more pronounced for the Y-doped spinel, as shown in Fig. 11. However, SEM images in Fig. 11 only provide qualitative insights into the fracture behavior. For this reason, the frequency of crack deflections was quantified and normalized by the total crack length. Crack deflections were considered

as changes in the trajectory of the crack. Crack deflections occurred every 7.5 μm (95% confidence interval is ± 2.7 μm) for undoped spinel, 6.5 μm (95% confidence interval is ± 0.9 μm) for Ca-doped spinel and 5.5 μm (95% confidence interval is ± 1.7 μm) for Y-doped spinel. A critical review of the EBSD maps revealed that some of the crack deflections occurred due to intergranular cracking, while other deflections corresponded to changes in the crack path after encountering a grain boundary between two adjacent grains with transgranular fracture (Fig. 3S). Both intergranular and transgranular fractures contributed to the tortuosity of the crack path.

The percentage of transgranular fracture for the undoped and Y-doped samples after annealing was very similar, as shown in Fig. 13a. Only the Ca-doped spinel sample after annealing presented a slightly lower percentage of transgranular fraction that could be related to the slightly smaller average grain size (860 nm for Ca-doped vs 1160 nm and 1180 nm for undoped and Y-doped spinel, respectively). The effect of grain size on the transgranular fracture can be more clearly seen when comparing any of the samples in the as-hot-pressed condition with the samples after annealing. Because of the smaller grain size, samples in the as-hot-pressed condition have a higher density of grain boundaries and consequently, a higher probability of the crack path encountering a grain boundary. As a result, the fraction of intergranular fracture was higher in the samples after hot-pressing (in which the grain sizes were smaller) as compared to the annealed samples. Transgranular fracture was more dominant than intergranular fracture in all the samples after annealing (~ 70% of the crack path length). Moreover, there was a decrease in the microhardness after annealing for all samples compared to the as-hot-pressed conditions due to grain growth, as shown in Fig. 13b.

Calcium and yttrium doping increased the indentation fracture toughness for the samples after annealing, as indicated in Fig. 13c. As mentioned earlier, crack deflections were more frequent in samples doped with calcium and yttrium resulting in a more tortuous crack propagation path in these samples. Thus, the enhanced indentation fracture toughness in calcium and yttrium was mainly due to the tortuous crack propagation path. Despite most crack deflections being associated with intergranular fracture in undoped and doped samples (81%-88% of the total number of deflections), Ca- and Y-doped samples presented no significant predominance of intergranular fracture when compared to undoped spinel (Table 1). Crack deflections have a toughening effect as they are responsible for a reduction in the stresses and strains experienced by the crack tip, impairing the crack propagation [55, 56]. Evidence of these toughening mechanisms has been found by Kueck et al. on Y- and Yb-doped SiC, where the segregation of yttrium and ytterbium at grain boundaries was a determinant factor for the occurrence of intergranular cracking associated with an enhanced fracture toughness [57].

In complex oxides such as spinel where 2 different cation sublattices exist, the elemental deviation of host cations must be also verified when discussing the grain-boundary cohesion. The aggravation of the non-stoichiometric composition at grain boundaries after doping, especially an excessive depletion of one or both host cations, could lead to weaker boundaries due to dangling bonds at the interface. As can be seen in Fig. 14a, the magnesium depletion is reduced after calcium doping compared to the undoped spinel. Additionally, yttrium doping

Table 1 Summary of crack length, crack deflection frequency and deflections associated with inter/transgranular cracking for undoped, Ca-doped and Y-doped spinel after annealing at 1400 °C for 48 h in N_2/H_2

	Crack length (μm (99% confidence level))	Crack deflection frequency (Deflections/ μm (95% confidence level))	Deflections associated with intergranular fracture (%)	Deflections associated with transgranular fracture (%)
Undoped Spinel	77.8 (± 1.1)	7.5 (± 2.7)	83	17
Ca-doped spinel	74.1 (± 1.1)	6.5 (± 0.9)	88	12
Y-doped spinel	73.6 (± 1.0)	5.5 (± 1.7)	81	19

decreases the aluminum excess at the grain boundary (Fig. 14a), but no significant depletion of magnesium or aluminum is observed at grain boundaries. Therefore, the mechanical integrity of grain boundaries is not compromised by excessive depletion of host cations, supporting the observation that no preferential intergranular fracture was found in Ca- and Y-doped samples compared to the undoped spinel condition. However, a thorough investigation of the grain-boundary strength and fracture toughness of individual grain boundaries coupled with quantitative XEDS and EELS analysis is necessary to directly correlate the segregation behaviors of calcium and yttrium and the mechanical properties of a particular grain boundary in spinel.

Conclusions

The effect of calcium and yttrium doping on the grain-boundary segregation behavior, fracture behavior, and bulk mechanical properties in spinel was quantitatively assessed in this study. The main insights derived from this work can be summarized as follows:

(1) The grain-boundary plane distributions of the doped and undoped samples after annealing were very similar. A slightly higher tendency for grain boundaries terminating in {111} planes was observed in all cases and more so for yttrium doped spinel. The population of grain-boundary planes with rotations about the [111] axis in Ca- and Y-doped samples were distinct compared to undoped spinel. In undoped spinel, the frequency of twist boundaries about the [111] axis was significantly dominant as compared to the tilt boundaries. In contrast, pure twist boundaries were found less frequently, and pure tilt boundaries were more prominent after calcium and yttrium doping compared to undoped spinel. This decrease in grain-boundary plane anisotropy can be attributed to the larger excess free volume of tilt boundaries compared to twist boundaries, allowing the accommodation of large calcium and yttrium cations at the boundary.
(2) Detailed quantitative spectrometry analysis by EELS and XEDS indicated that Ca^{2+} cations preferentially occupy Mg^{2+} sites, while Y^{3+} preferentially replaces Al^{3+} at grain boundaries in spinel. Direct observations of individual yttrium atoms at the grain boundaries confirmed the substitution of Al^{3+} by Y^{3+}. Additionally, the maximum segregation levels observed were 0.8 ± 0.1 calcium atoms/nm^2 (0.23 ± 0.03 monolayers) and 2.4 ± 0.06 yttrium atoms/nm^2 (0.45 ± 0.11 monolayers), respectively.
(3) Both calcium and yttrium doping effectively increased the indentation fracture toughness of spinel compared to the undoped condition. The enhanced fracture toughness was attributed to more prominent crack deflections and a more tortuous crack path in the Ca- and Y-doped samples compared to the undoped spinel.

Acknowledgements

This work was supported by the National Science Foundation through grants CMMI-2016279, DMR-2018683, and DMR-2215267. The authors wish to acknowledge the insightful discussions with Dr. Gregory Rohrer regarding quantitative EBSD analysis.

Author contributions

Alexander Campos-Quiros: Conceptualization, Methodology, Software, Validation, Formal Analysis, Investigation, Data Curation, Writing—Original Draft, Visualization. Metri Zughbi: Methodology, Software, Validation, Formal Analysis, Investigation, Data Curation. Animesh Kundu: Conceptualization, Methodology, Validation, Investigation, Resources, Writing—Review and Editing, Supervision, Project Administration, Funding Acquisition. Masashi Watanabe: Conceptualization, Methodology, Software, Validation, Investigation, Resources, Writing—Review and Editing, Supervision, Project Administration, Funding Acquisition.

Data availability

The data that support the findings of this study are available from the corresponding author upon reasonable request.

Declarations

Conflict of interest The authors declare that they have no known competing financial interests or personal relationships that could have appeared to influence the work reported in this paper.

Ethical approval Not applicable.

Supplementary Information The online version contains supplementary material available at https://doi.org/10.1007/s10853-024-10569-9.

References

[1] Rubat du Merac M, Kleebe HJ, Müller MM, Reimanis IE (2013) Fifty years of research and development coming to fruition; unraveling the complex interactions during processing of transparent magnesium aluminate ($MgAl_2O_4$) spinel. J Am Ceram Soc 96:3341–3365. https://doi.org/10.1111/jace.12637

[2] Ganesh I (2013) A review on magnesium aluminate ($MgAl_2O_4$) spinel: synthesis, processing and applications. Int Mater Rev 58:63–112. https://doi.org/10.1179/1743280412Y.0000000001

[3] Miller J, Reimanis I, Miao W, Salem J (2017) Mechanical and optical properties in precipitated regions of alumina-rich magnesium aluminate spinel. Int J Appl Ceram Technol 14:236–244. https://doi.org/10.1111/ijac.12644

[4] Rösler J, Harders H, Bäker M (2007) Mechanical behaviour of engineering materials: metals, ceramics, polymers, and composites. Springer, New York

[5] Gibson MA, Schuh CA (2015) Segregation-induced changes in grain boundary cohesion and embrittlement in binary alloys. Acta Mater 95:145–155. https://doi.org/10.1016/j.actamat.2015.05.004

[6] Bokov A, Zhang S, Feng L, Dillon SJ, Faller R, Castro RHR (2018) Energetic design of grain boundary networks for toughening of nanocrystalline oxides. J Eur Ceram Soc 38:4260–4267. https://doi.org/10.1016/j.jeurceramsoc.2018.05.007

[7] Feng L, Hao R, Lambros J, Dillon SJ (2018) The influence of dopants and complexion transitions on grain boundary fracture in alumina. Acta Mater 142:121–130. https://doi.org/10.1016/j.actamat.2017.09.002

[8] Cao W, Kundu A, Yu Z, Harmer MP, Vinci RP (2013) Direct correlations between fracture toughness and grain boundary segregation behavior in ytterbium-doped magnesium aluminate spinel. Scr Mater 69:81–84. https://doi.org/10.1016/j.scriptamat.2013.03.002

[9] Müller MM, Kleebe HJ (2012) Sintering mechanisms of LiF-doped Mg-Al-spinel. J Am Ceram Soc 95:3022–3024. https://doi.org/10.1111/j.1551-2916.2012.05413.x

[10] Schumacher O, Marvel CJ, Kelly MN, Cantwell PR, Vinci RP, Rickman JM, Rohrer GS, Harmer MP (2016) Complexion time-temperature-transformation (TTT) diagrams: opportunities and challenges. Curr Opin Solid State Mater Sci 20:316–323. https://doi.org/10.1016/j.cossms.2016.05.004

[11] Bojarski SA, Stuer M, Zhao Z, Bowen P, Rohrer GS (2014) Influence of y and la additions on grain growth and the grain-boundary character distribution of alumina. J Am Ceram Soc 97:622–630. https://doi.org/10.1111/jace.12669

[12] Baruah B, Sarkar R (2023) Effect of Y_2O_3 content on densification, microstructure and mechanical properties of reaction sintered magnesium aluminate spinel. Ceram Int 49:755–765. https://doi.org/10.1016/j.ceramint.2022.09.047

[13] Boch P, Niepce J-C (2007) Ceramic materials: processes, properties and applications. ISTE USA, USA

[14] Kang S-JL (2005) Grain boundary segregation and grain boundary migration. In: Sintering. Elsevier, pp 97–103.

[15] Cui FY, Kundu A, Krause A, Harmer MP, Vinci RP (2018) Surface energies, segregation, and fracture behavior of magnesium aluminate spinel low-index grain boundary planes. Acta Mater 148:320–329. https://doi.org/10.1016/j.actamat.2018.01.039

[16] Shannon RD (1976) Revised effective ionic radii and systematic studies of interatomic distances in halides and chalcogenides. Acta Crystallog Sect A 32:751–767. https://doi.org/10.1107/S0567739476001551

[17] Marvel CJ, Krause AR, Harmer MP (2021) Effect of Eu-doping and grain boundary plane on complexion transitions in $MgAl_2O_4$. J Am Ceram Soc 104:4203–4213. https://doi.org/10.1111/jace.17831

[18] Chiang Y-M, David Kingery W (1990) Grain-boundary migration in nonstoichiometric solid solutions of magnesium aluminate spinel: II, effects of grain-boundary nonstoichiometry. J Am Ceram Soc 73:1153–58. https://doi.org/10.1111/j.1151-2916.1990.tb05172.x

[19] Syed K, Xu M, Ohtaki KK, Kok D, Karandikar KK, Graeve OA, Bowman WJ, Mecartney ML (2020) Correlations of grain boundary segregation to sintering techniques in a three-phase ceramic. Materialia 14:100890. https://doi.org/10.1016/j.mtla.2020.100890

[20] Kim JM, Kim HN, Park YJ, Ko JW, Lee JW, Kim HD (2016) Microstructure and optical properties of transparent $MgAl_2O_4$ prepared by Ca-infiltrated slip-casting and

sinter-HIP process. J Eur Ceram Soc 36:2027–2034. https://doi.org/10.1016/j.jeurceramsoc.2016.02.018

[21] Thomas R (1971) Free energy of formation of binary compounds. MIT Press, Cambridge MA

[22] Yi S, Huang Z, Huang J, Fang M, Liu Y, Zhang S (2014) Novel calcium hexaluminate/spinel-alumina composites with graded microstructures and mechanical properties. Sci Rep 4:4333. https://doi.org/10.1038/srep04333

[23] Liu J, Wang Z, Liu H, Wang X, Ma Y (2020) Effect of Y_2O_3 doping on the high-temperature properties of magnesia aluminate spinel refractories. J Aust Ceram Soc 56:389–394. https://doi.org/10.1007/s41779-019-00340-8

[24] West GD, Perkins JM, Lewis MH (2004) Characterisation of fine-grained oxide ceramics. J Mater Sci 39:6687–6704. https://doi.org/10.1023/B:JMSC.0000045600.77776.08

[25] Campos-Quiros A, Zughbi M, Kundu A, Watanabe M (2024) Quantitative analysis of grain boundary segregation and fracture behavior in Ca-doped magnesium aluminate spinel. J Mater Sci 59:16862–16883. https://doi.org/10.1007/s10853-024-10171-z

[26] Wright SI (2006) Random thoughts on non-random misorientation distributions. Mater Sci Technol 22:1287–1296. https://doi.org/10.1179/174328406X130876

[27] Saylor DM, El-Dasher BS, Adams BL, Rohrer GS (2004) Measuring the five-parameter grain-boundary distribution from observations of planar sections. Metall Mater Trans A 35A:1981–1989. https://doi.org/10.1007/s11661-004-0147-z

[28] Saylor DM, Rohrer GS (2002) Determining crystal habits from observations of planar sections. J Am Ceram Soc 85:2799–2804. https://doi.org/10.1111/j.1151-2916.2002.tb00531.x

[29] Rohrer GS, Randle V, Kim CS, Hu Y (2006) Changes in the five-parameter grain boundary character distribution in α-brass brought about by iterative thermomechanical processing. Acta Mater 54:4489–4502. https://doi.org/10.1016/j.actamat.2006.05.035

[30] Rohrer GS (2011) Grain boundary energy anisotropy: a review. J Mater Sci 46:5881–5895. https://doi.org/10.1007/s10853-011-5677-3

[31] Watanabe M, Williams DB (2003) Quantification of elemental segregation to lath and grain boundaries in low-alloy steel by STEM X-Ray mapping combined with the ζ-factor method. Z Metallkd 94:307–316. https://doi.org/10.3139/146.030307

[32] Watanabe M, Williams DB (2006) The quantitative analysis of thin specimens: a review of progress from the Cliff-Lorimer to the new ζ-factor methods. J Microsc 221:89–109. https://doi.org/10.1111/j.1365-2818.2006.01549.x

[33] Watanabe M, Egerton RF (2022) Evolution in X-ray analysis from micro to atomic scales in aberration-corrected scanning transmission electron microscopes. Microscopy 71:I132–I147. https://doi.org/10.1093/jmicro/dfab026

[34] Watanabe M, Okunishi E, Ishizuka K (2009) Analysis of spectrum-imaging datasets in atomic-resolution electron microscopy. Microsc Anal 23:5–7

[35] Egerton RF (2011) Electron energy-loss spectroscopy in the electron microscope. Springer, US

[36] ASTM Standard C1327–15 (2019) Standard Test Method for Vickers Indentation Hardness of Advanced Ceramics. ASTM International, West Conshohocken, PA

[37] Miyoshi T, Sagawa N, Sassa T (1985) Study on fracture toughness evaluation for structural ceramics. Trans Jpn Soc Mech Eng A 51:2489–2497. https://doi.org/10.1299/kikaia.51.2489

[38] Pennycook SJ, Nellist PD (2011) Scanning transmission electron microscopy. Springer, New York

[39] Momma K, Izumi F (2011) VESTA 3 for three-dimensional visualization of crystal, volumetric and morphology data. J Appl Crystallogr 44:1272–1276. https://doi.org/10.1107/S0021889811038970

[40] De Aza AH, Pena P, De Aza S (1999) Ternary system Al_2O_3-MgO-CaO: I, primary phase field of crystallization of spinel in the subsystem $MgAl_2O_4$-$CaAl_4O_7$-CaO-MgO. J Am Ceram Soc 82:2193–2203. https://doi.org/10.1111/j.1151-2916.1999.tb02062.x

[41] Tomsia AP, Glaeser AM (1998) Ceramic microstructures: control at the atomic level. Springer Science+Business Media, New York

[42] Romig ADJ, Goldstein JI (1979) Detectability limit and spatial resolution in STEM X-ray analysis: application to Fe-Ni. In: Newbury DE (ed) Microbeam Analysis—1979. San Francisco Press, San Francisco, CA, pp 124–128

[43] Halabi M, Ezersky V, Kohn A, Hayun S (2017) Charge distribution in nano-scale grains of magnesium aluminate spinel. J Am Ceram Soc 100:800–811. https://doi.org/10.1111/jace.14610

[44] Nuns N, Béclin F, Crampon J (2009) Grain-boundary characterization in a nonstoichiometric fine-grained magnesium aluminate spinel: effects of defect segregation at the space-charge layers. J Am Ceram Soc 92:870–875. https://doi.org/10.1111/j.1551-2916.2008.02901.x

[45] Rufner JF, Kaseman D, Castro RHR, Van Benthem K (2016) DC Electric field-enhanced grain-boundary mobility in magnesium aluminate during annealing. J Am Ceram Soc 99:1951–1959. https://doi.org/10.1111/jace.14157

[46] Zubrzycka P, Radecka M, Graule T, Trenczek-Zając A, Zientara D, Stuer M (2024) $MgAl_2O_4$ spinel with

transmittance approaching theoretical value at reduced sintering temperatures. J Eur Ceram Soc 44:6047–6059. https://doi.org/10.1016/j.jeurceramsoc.2024.03.049

[47] Read WT (1953) Dislocations in crystals. McGraw-Hill Book Company Inc, York, PA

[48] Aaron HB, Bolling GF (1972) Free volume as a criterion for grain boundary models. Surf Sci 31:27–49. https://doi.org/10.1016/0039-6028(72)90252-X

[49] Miller HM, Saylor D, El Dasher BS, Rollett AD, Rohrer GS (2004) Crystallographic distribution of internal interfaces in spinel polycrystals. Mater Sci Forum 467–470:783–788. https://doi.org/10.4028/www.scientific.net/MSF.467-470.783

[50] Saylor DM, Morawiec A, Rohrer GS (2003) The relative free energies of grain boundaries in magnesia as a function of five macroscopic parameters. Acta Mater 51:3675–3686. https://doi.org/10.1016/S1359-6454(03)00182-4

[51] Kaplan WD, Chatain D, Wynblatt P, Carter WC (2013) A review of wetting versus adsorption, complexions, and related phenomena: the rosetta stone of wetting. J Mater Sci 48:5681–5717. https://doi.org/10.1007/s10853-013-7462-y

[52] Hasan MM, Dholabhai PP, Dey S, Uberuaga BP, Castro RHR (2017) Reduced grain boundary energies in rare-earth doped $MgAl_2O_4$ spinel and consequent grain growth inhibition. J Eur Ceram Soc 37:4043–4050. https://doi.org/10.1016/j.jeurceramsoc.2017.04.073s

[53] Benameur N, Bernard-Granger G, Addad A, Raffy S, Guizard C (2011) Sintering analysis of a fine-grained alumina-magnesia spinel powder. J Am Ceram Soc 94:1388–1396. https://doi.org/10.1111/j.1551-2916.2010.04271.x

[54] Stewart RL, Bradt RC (1980) Fracture of polycrystalline $MgAl_2O_4$. J Am Ceram Soc 63:619–623. https://doi.org/10.1111/j.1151-2916.1980.tb09847.x

[55] Ritchie RO (2021) Toughening materials: enhancing resistance to fracture. Phil Trans R Soc A 379:20200437. https://doi.org/10.1098/rsta.2020.0437

[56] Ritchie RO (2011) The conflicts between strength and toughness. Nat Mater 10:817–822. https://doi.org/10.1038/nmat3115

[57] Kueck AM, Kim DK, Ramasse QM, De Jonghe LC, Ritchie RO (2008) Atomic-resolution imaging of the nanoscale origin of toughness in rare-earth doped SiC. Nano Lett 8:2935–2939. https://doi.org/10.1021/nl8017884